Bio-Inspired Design and Fabrication of a Spectrally Resolved Albedometer

Ana Romero Olvera

TUDelft

Bio-Inspired Design and Fabrication of a Spectrally Resolved Albedometer

By

Ana Romero Olvera

in partial fulfilment of the requirements for the degree of

Master of Science
in Sustainable Energy Technology

at the Delft University of Technology,
to be defended publicly on Thursday September 16, 2021, at 10:00 AM.

Supervisor:	Dr. Hesan Ziar
Thesis committee:	Prof. Dr. Olindo Isabella, TU Delft
	Dr. Jeremy Faludi, TU Delft
	Ir. Arturo Martinez, TU Delft

This thesis is confidential and cannot be made public until September 16, 2023.

An electronic version of this thesis is available at http://repository.tudelft.nl/

I. Abstract

With the increased market share of bifacial modules, it is becoming increasingly important to have sensors that provide information about the irradiance falling into both sides of the modules. Such instruments give more information about the performance of PV modules. They can optimize the material, tilt, and orientation of PV modules according to the surface on which they are installed. However, most sensors in the market do not provide spectrally resolved data, and the ones they do can be expensive.

Because of the preceding, this thesis aimed to design and fabricate a cost-effective spectrally resolved albedometer that will measure the global and reflected irradiance in three different parts of the solar spectrum using photodiodes as sensing elements. This thesis demonstrates how the device's optical, electrical, and mechanical characteristics can be optimized to obtain a more accurate estimation of the spectral albedo.

Additionally, a bio-inspired casing design with self-shading properties was created to reduce the temperature inside the device. Two prototypes were fabricated with two different colour-diffuser configurations (Grey-N-BTK diffuser and White-Hybrid diffuser). Data measured by the final prototypes was calibrated and validated with measurements from an EKO MS700 spectroradiometer. The final sensors have an average error of 20.4% and 7.3% and operate at 17ºC and 8.6ºC above ambient temperature. The albedometers have a volume of 810 cm^2 and cost around €978.

Contents

1. Introduction

Due to the continuous increase of energy demand, ensuring the energy supply has become a global challenge, especially with the expected scarcity of fossil fuels, which still account for most of the energy market in the world. The Sun is a significant source of free energy. Theoretically, solar energy can fulfil the entire world's energy demand if technologies are further developed [1]. Additionally, solar energy is associated with the global goal to reduce global carbon emissions. Therefore, adopting solar technologies such as photovoltaic technologies would mitigate energy supply security, climate change, and other economic issues.

1.1. Bifacial PV

Due to the potential of solar technologies for energy supply security and climate change mitigation, Photovoltaic technologies have increased their presence in the energy market. Bifacial solar cells are characterized by their ability to convert incident radiation falling onto both the front and rear sides of the cell. If bifacial cells are mounted in a PV module using a transparent rear cover, these modules can increase their energy yield. Up to 13 to 35 per cent higher than monofacial modules under sunny conditions and from 40 to 70 per cent under cloudy conditions, depending on various factors such as height, module, tilt and albedo [2]. According to the International Technology Roadmap for Photovoltaic

(ITRPV), the bifacial modules market share is proliferating within PV technologies. It is predicted to increase to more than 50 per cent within the next 20 years (Figure 1).
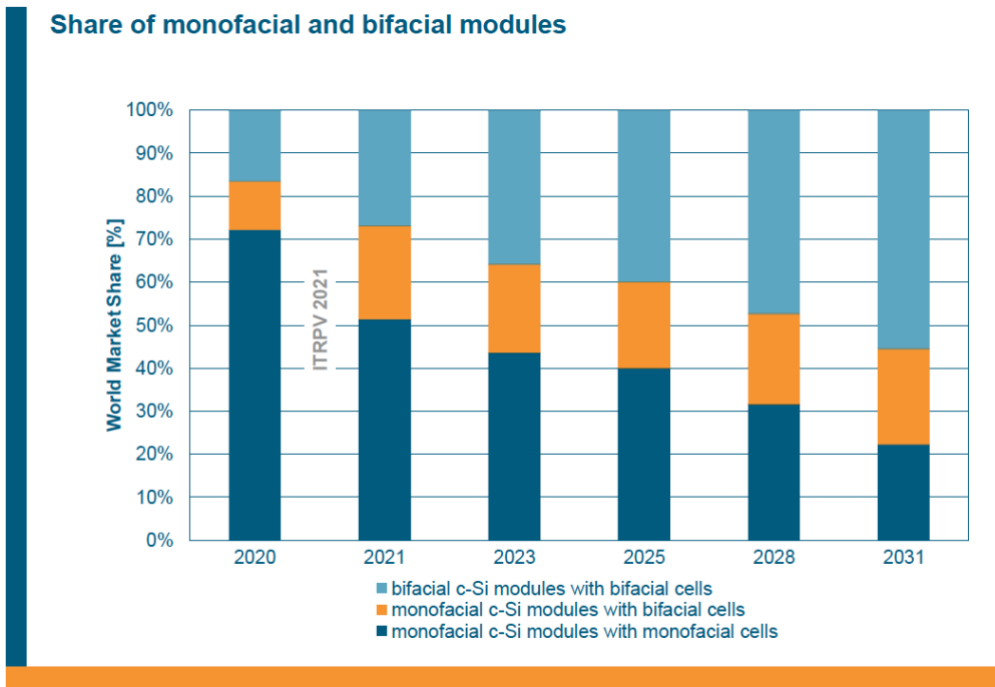

Figure 1: Share of monofacial and bifacial modules taken from the International Technology Roadmap for photovoltaic [3] forecasts a continuous increase in bifacial modules (with bifacial cells) market share, taking up to 50% of the market by 2031.

1.2.   Spectral Albedo

The albedo is the fraction of light that a given surface reflects, given as the ratio between the power of the reflected light and the total incoming light [2]. The albedo is not an intrinsic property of materials because it is dependent on the directional and spectral conditions of sunlight [4]. Bifacial modules benefit from the spectral albedo since it improves their performance according to the reflected light on the rear side of the module. The albedo can also influence the performance of monofacial modules if installed at high tilt angles or as vertical building-integrated PV systems and other non-PV related activities such as meteorological and agricultural applications.
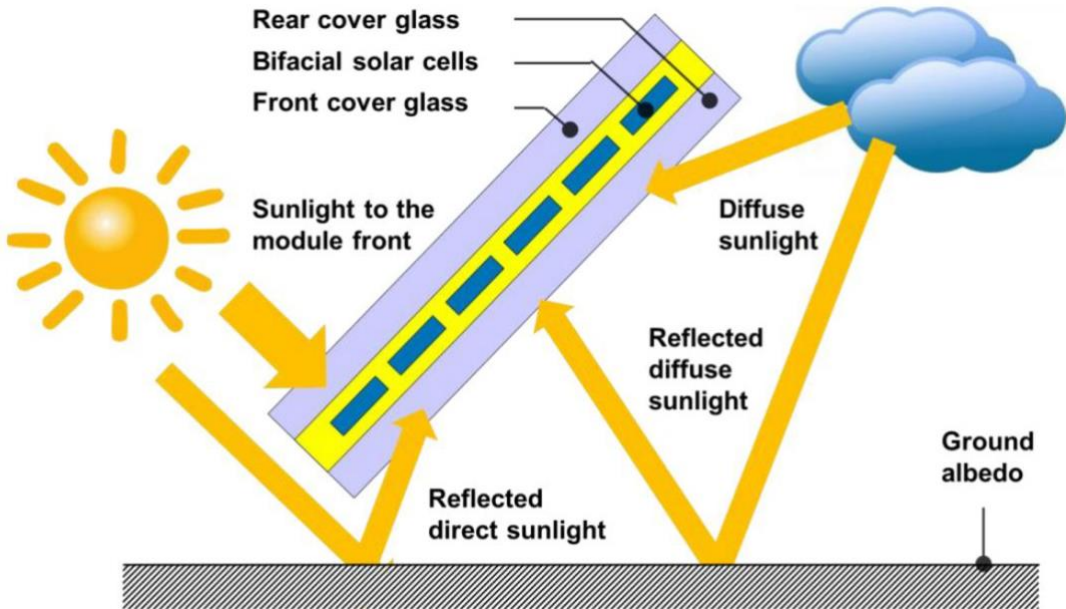
Figure 2: Light incident on a bifacial module [5]

Ignoring the spectral dependence of the albedo can impact the optimal selection of PV materials since it has been found that certain ground surfaces have bias reflectivity towards specific wavelengths, which can lower the performance of PV cells [4]. For example, snow has an albedo of 0.96 to 0.98 between 200 and 700 nm meaning that the reflected light corresponds to the near-UV and visible spectrum [6]. The solar cell's performance will be optimal if one uses materials as a-Si:H, which operates at wavelengths where the snow showed the highest albedo values (See the highlighted area in Figure 3). However, suppose the same material is placed on a grass surface, with its higher albedo value at wavelengths over 700 nm. In that case, the light reflected by the surface will be at wavelengths outside of the operation range of the material and thus, not absorbed, reducing the module's performance at this specific surface. In this case, choosing another material, such as c-Si, will yield a greater albedo since c-Si does operate at those ranges.
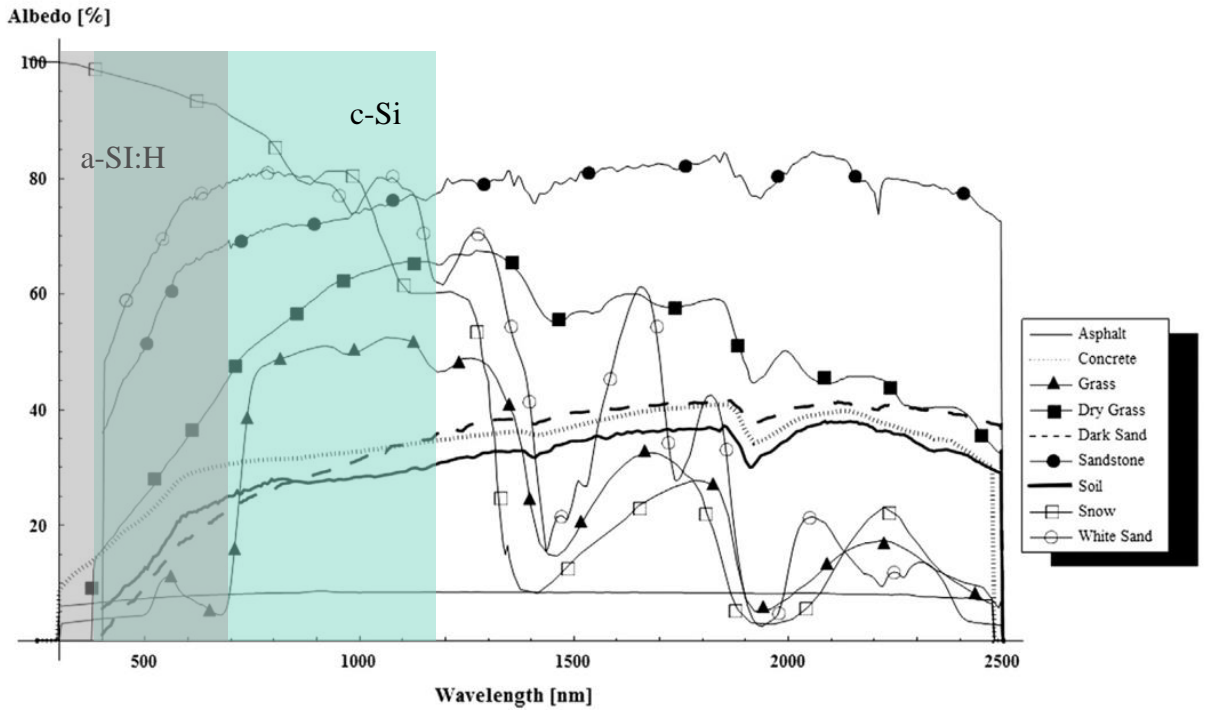
Figure 3: Comparison of Spectral albedo for different materials for industrial PV applications and spectral responsivity range of a-Si:H and c-Si adapted from [7]

The albedo is often averaged over the solar spectrum for the diverse ground materials. When this is done, the wavelength-specific characteristic of the albedo is ignored, leading to a lower accuracy on the current prediction of the power output of bifacial PV modules. The optimal operating conditions and the efficiency of the PV systems can change significantly to those using spectral albedo [2]. For instance, in green grass, the power outputs are increased by 3.1% when taking a spectrally dependent albedo into account [2]. Consequently, having a device that measures the spectrally resolved albedo is essential.

1.3. Design Requirements

The irradiance sensor (V1) designed and built by Annanta Kaul in 2020 (Figure 4) was the starting point for the design of the present albedometer. The first version of the sensor is a pyranometer that measures solar irradiance in three different wavelength ranges (300-700nm, 700-900nm, 900-1100nm) of the solar spectrum using silicon photodiodes as

sensing elements and optical filters to separate the spectrum. A diffuser is used to provide a uniform cosine response. The device weighs 1.02 kg, has a volume of 122x120x80 mm3 and cost €345 [8].
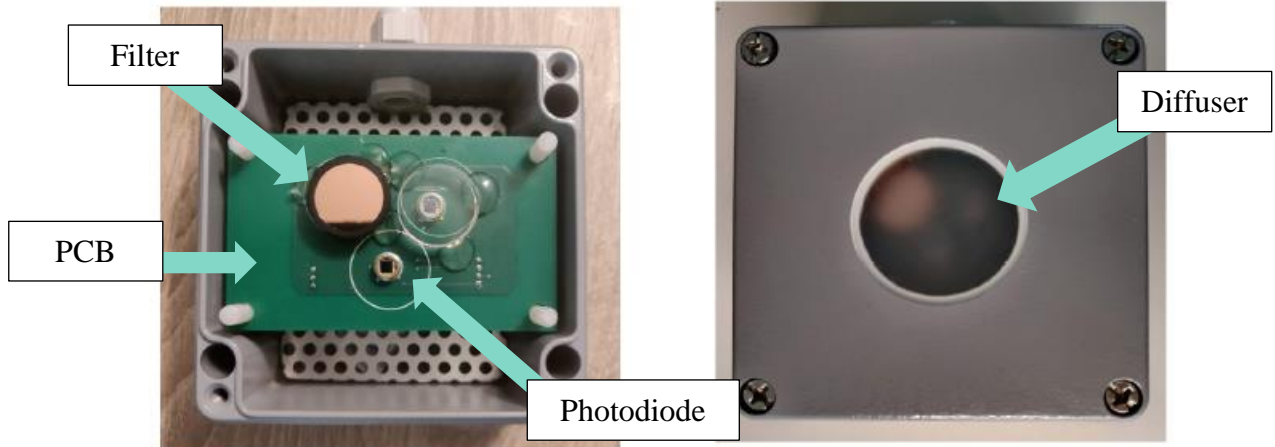
Figure 4: Irradiance Sensor designed by Annanta Kaul [8]

After revising Kaul's work, several limitations on the performance of the device were found. In terms of the optical design, first, Kaul mentions that the diffuser has good transmittance [8]. However, it exhibits undesirable specular transmittance, limiting the reliability of measurements. Second, the sensor has an angular dependency. This results in inconsistencies in the measured irradiance depending on the device's position towards the light source (azimuth). Finally, optical filters do not separate the spectrum in the claimed wavelength ranges and adds the irradiance between 320nm and 350nm to the measurements in the 700-900nm range.

In V1, the filters had a diameter of 25.4 mm and could not be cut. The filter diameter imposed a constraint on the spacing of the photodiodes. The physical contact between adjacent filters limited the space. Therefore, the size of the PCB was kept large. The size of the PCB will further cause a restriction in the minimum size of the casing. A significant restriction was the distance between the sensing elements and the diffuser. A larger distance between photodiodes and diffuser leads to additional optical issues. A list of requirements to solve these inconveniences was created and analysed next for all these limitations.

House of Quality

A House of Quality (HoQ) matrix was created to solve the problems found in the V1 sensor. An HoQ provides a conceptual map for establishing priorities of the design requirements previously deducted from customer and functional requirements [9]. This matrix is mainly used to translate customer needs and desires into technical design requirements to increase their satisfaction [9]. Consequently, the main components of an HoQ are design (columns) and customer (rows) requirements, the relation between the requirements, and the correlation between the functional (design) requirements on top. Typically, an HoQ employs a rating scale to evaluate the degree of importance and strength between customer requirements and functional requirements [9].
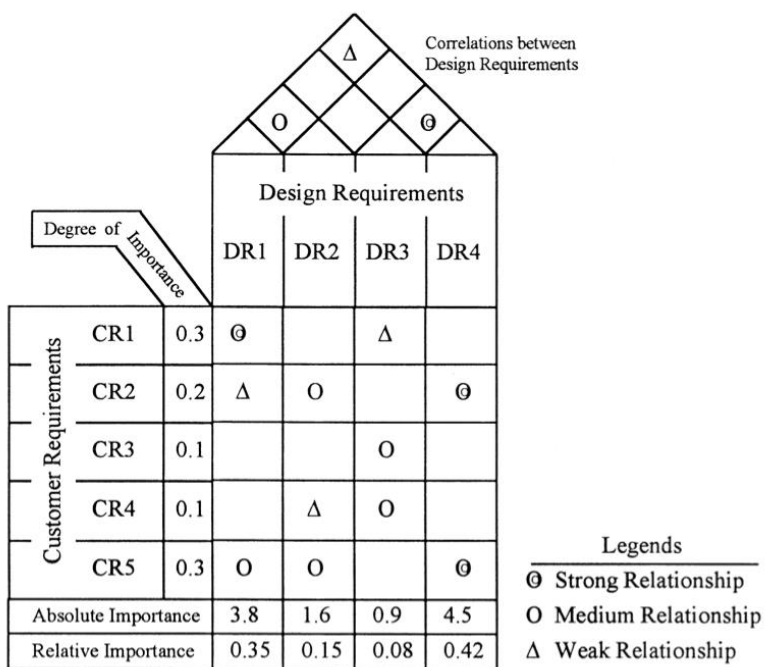

Figure 5: HOQ matrix scheme showing its main components [9]

The approach for building the HoQ was done following "Determination of an Optimal Set of Design Requirements Using House of Quality."[9]. o establish the priorities of the design requirements through the HoQ, the following steps were followed. First, the customer requirements (CR) and Design requirements (DR) for the albedometer were obtained from the problems found in Annanta's version of the sensor, literature, and

current sensors in the market. Second, the relation between both CR and DR were categorized as strong, moderate or weak.

Third, the correlations between all DR were established as positive, negative or no correlation indicating the direction of improvement (i.e., whether the DR had to be minimized, maximize, or achieve a specific target) of each DR. Next, the degree strength between CR and DR was evaluated with a scaling rating (i.e., 1,3,9); the more significant the relation between requirements, the bigger the rating. Moreover, the customer importance was rated on a scale of one to five. Finally, the relative weight (1) of all requirements was computed to obtain the requirements one should prioritize. A higher relative weight is given to functional requirements strongly related to customer requirements with higher importance. The matrix created for this analysis corresponds to Figure 6.

$$Relative\ weight\ = \frac{Customer\ Importance}{\sum Customer\ Importance\ \cdot\ Number\ of\ CR} \qquad (1)$$
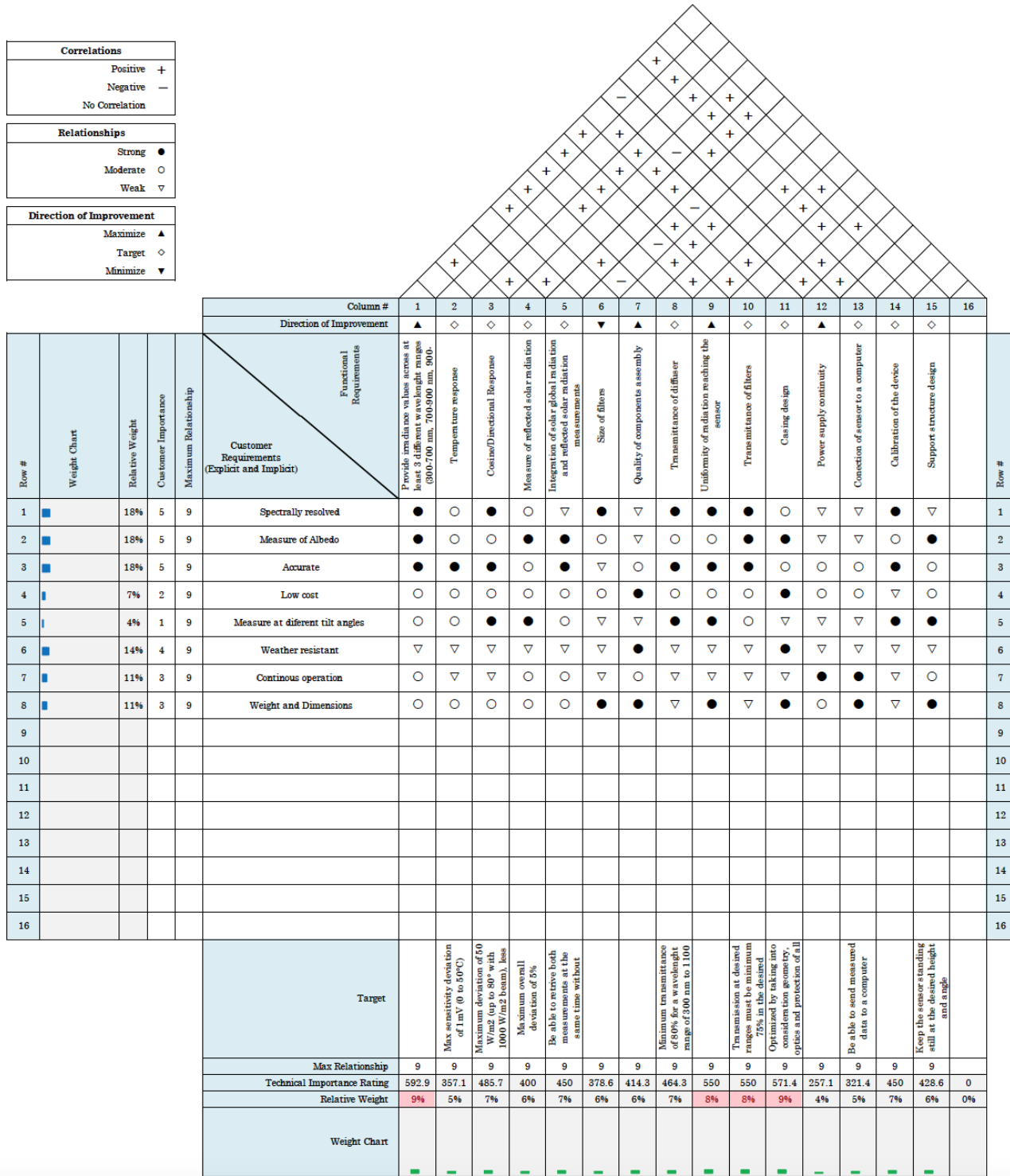
Figure 6: House of Quality for the design of the albedometer. Desing Requirements are shown as Functional Requirements in the matrix.

From the House of Quality presented in Figure 6, it was concluded that the customer requirements with higher importance (highest relative weight) are:

- Spectrally resolved characteristic
- Measure of albedo (both global and reflected irradiance)

- Improve device's accuracy

Consequently, the main functional requirements to focus on are:

- Providing irradiance values across at least three different wavelength ranges
- Uniformity of radiation reaching the sensor
- Transmittance of filters (Optical properties)
- Casing design

1.4. Working Principle

The final instrument consists of an up-facing sensor (facing the sky) and a down-facing sensor (facing the ground). Both sensors are spectrally resolved, providing wavelength-specific measurements of incoming global and reflected irradiance. The main components of the device are the diffusers, optical filters, photodiodes (sensing elements), printed circuit boards, and an interface that retrieves and save the collected data. The flowchart in Figure 7 shows how the albedometer measures the incoming light and estimates the spectral albedo.
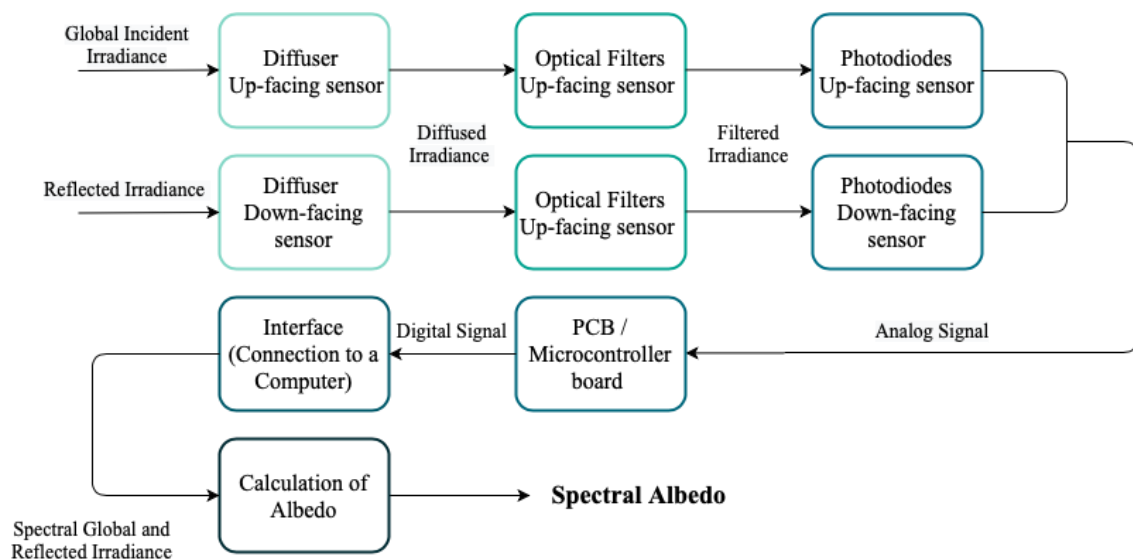

Figure 7: Working Flowchart of Albedometer showing how the Spectral Albedo is estimated from the measured incident global and reflected irradiance

1.5.   Aim and Outline

To better understand the behaviour of bifacial PV and a more accurate prediction of their energy yield, a sensor capable of gathering spectrally resolved data from both global and reflected irradiance is needed. This information can provide an accurate dependency of modules to albedo. It can be used to optimise the PV modules' materials, tilt angle, or orientation for specific environmental conditions.

The albedo is mainly measured using two pyranometers, which only provide the averaged irradiance for all wavelengths. This option will not provide enough information to provide an accurate prediction of the performance of modules. Another option is implementing two spectroradiometers on each module's side, which provides spectrally resolved data. However, spectroradiometers are very expensive, and it would not be practical to have them on every system. Consequently, the objective of this thesis is to design and fabricate a cost-effective spectrally resolved albedometer. This sensor will be presented as the second version of the irradiance sensor (V1) built by Annanta Kaul in 2020 [8]. It aims to increase the accuracy of the device while improving its optical, electrical, and mechanical characteristics.

The outline of the report is as follows. In Chapter 2, the theoretical framework of irradiance sensors and albedometers will be discussed. A market analysis of current and future technologies and applications will be discussed, followed by the methodology for the work presented in this thesis. In Chapter 4, the improvements to the optical design in comparison to V1.0 will be analysed. Chapter 3 will give a brief explanation of the electrical design and the essential components of the device. Next, the mechanical design of the sensor will be explained in Chapter 5, including the bio-inspired casing design, temperature performance tests and the manufacturing process. Chapter 6 details the calibration procedure, followed by the validation of the calibration factors from outdoor conditions and calculation of the albedo presented in Chapter 7. Chapter 8 discusses all electrical, optical, and mechanical design components and the sensor overall performance and recommendations for future versions. Finally, Chapter 9 summarises the project.

2. Theoretical framework

2.1. Albedometers

As mentioned in Section 1.2, the albedo relates the power of the light reflected by a particular surface and the total incoming light. Due to the importance of albedo, albedometers are used to measure both global incident irradiance and ground reflected irradiance, which later can be used to estimate the albedo of a particular surface. Knowing the albedo of a surface can be an advantage for selecting materials, design, and analysis of PV technologies, as well as agricultural and meteorological implementations.

Figure 8: Spectrafy SolarSIM Albedometer consisting of two SolarSIM-G spectral irradiance sensors
[10].

Albedometers are typically composed of two pyranometers facing opposite directions, as seen in Figure 8. The up-facing pyranometer measures the global solar radiation, and the down-facing sensor measures the light reflected from the surface. However, most pyranometers in the market provide a single albedo value for the entire spectrum, ignoring the wavelength dependency of albedo. The solar sensors that provide multi-spectral measurements have very high prices and are not cost-effective to install in all systems.

2.2.   Sensors in the market

Some of the solar sensors in the market are compared in Table 1. These specifications were used to establish the customer requirements in Section 1.3 and will later be used to compare the present albedometer's performance to existing technologies. It is important to recall that none of the prices is accessible without a quotation. However, an albedometer composed of two EKO: MS-711 spectroradiometer is estimated to cost approximately €31,280 [8].

Table 1: Specifications of sensors in the market retrieved from technical specifications provided by the manufacturers

Specifications	EKO: MS-711 Spectroradiometer	Spectrafy: SolarSIM-ALB	Kipp & Zonen: CMP11 Albedometer	Hukseflux: SRA30-M2-D1 Albedometer
Classification	Class A	Class A	Class A	Class A
Spectrally resolved	Yes	Yes	No	No
Detector type	-	Silicon and InGaAs photodiodes	Thermopile	Thermopile
Wavelength range	300 – 1100 nm (50% Points)	280-4000 nm	285 – 2800 nm	285 – 3000 nm
Optical Resolution	< 7nm	+- 1 nm	-	
Response Time	-	0.7s	< 5s	
Maximum irradiance	-	2000 W/m2	4000 W/m2	-
Wavelength accuracy	+- 0.2 nm	+- 0.1 nm	-	-
Directional response at 1000 W/m2	<5 %	<1%	<1%	<0.5%
Temperature response	<2 %	<0.1%	<1%	< +- 0.4%
Operational temperature range	-10°C to 50°C	-30 °C to 65 °C	-40 °C – 80 °C	-40°C - 80°C
Exposure time	10-5000 msec	<1ms	-	
Dome material	Quartz	-	-	
Power supply	12VDC,50VA	12 VDC, <2W	-	12 VDC, <3W
Dimensions mm	220(D) x 197 (H) mm	132 x 132 x 250 mm	150 (D) x 68 (H)x 50 (d) MM	
Weight	4.5 kg	2.4 kg		

2.3. Methodology

As mentioned before, the present spectral albedometer is based on the irradiance sensor V1 designed by Annanta Kaul. To achieve an accurate estimation of the spectral albedo design requirements were defined in Section 1.3, considering problematic characteristics

of the V1 of the sensor, current market technologies, customer requirements and technical requirements. Modifications to V1 and new implementations will be divided into three main categories, Electrical Design, Optical Design, Mechanical Design. However, several components and modifications of each category are strongly related and dependent on each other.

Optical Design

Optimization of the optical design was marked as a priority during the HoQ analysis, specifically providing irradiance values across three different wavelength ranges, uniformity of radiation reaching the photodiodes and improving transmittance of filters.

Uniformity of light reaching the sensor was improved by selecting a new diffuser, optimization of the distance between the diffuser and photodiodes, and eliminating shadowing inside the device.

Additionally, these modifications reduced the reflected light inside the sensor, increased the sensor's minimum angle of incidence, and warranties that the light reaching the detectors after entering the device is maximized. Both providing the irradiance across three different wavelength ranges and good transmittance properties of filters were achieved by selecting new filters. The new filters provide sharper spectrum ranges while reducing their cost and size. Figure 9 summarizes how the requirements were addressed.
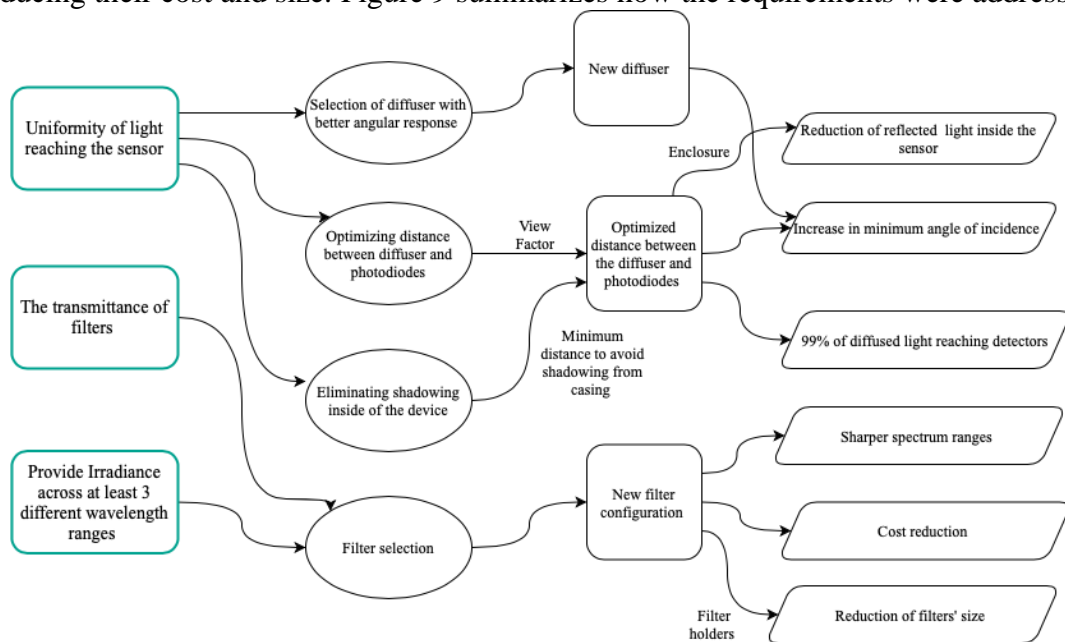

Figure 9: Main functional requirements addressed through optical design

Electrical Design

The reduction of the filters' size, design of filter holders and other modifications to the optical design played a major role in improving the electrical design. There were four major modifications to the electrical components in comparison to V1 of the solar sensor:

1. The PCBs were fabricated with a black material instead of green.
2. Due to the new smaller filters, it was possible to reduce the size of the sensing PCB and minimize the distance between the photodiodes. These changes improve both optical (uniformity) and mechanical properties of the sensor (casing design).
3. Incorporating a down-facing sensor to measure the reflected irradiance guarantees that the final instrument measures the albedo and not only the incoming global radiation.
4. A USB connection did the power supply continuity and connection to a computer to microcontroller in the PCB assembly.
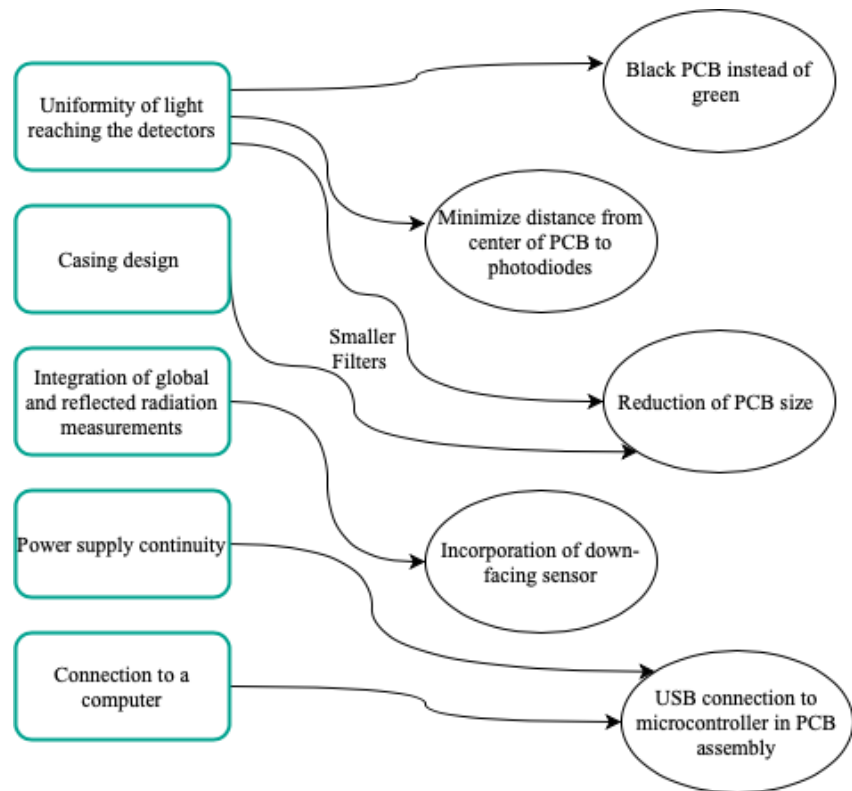
Figure 10: Modifications made to the electrical design that contribute to the achievement of functional requirements

Mechanical Design

The mechanical design focuses mainly on the casing design. However, it incorporates many functional and costumer requirements and the previously mentioned optical and electrical improvements during the process. Figure 11 illustrates how the casing design correlates with other functional requirements, the main factors considered for the design, and the general outcome from this new design.
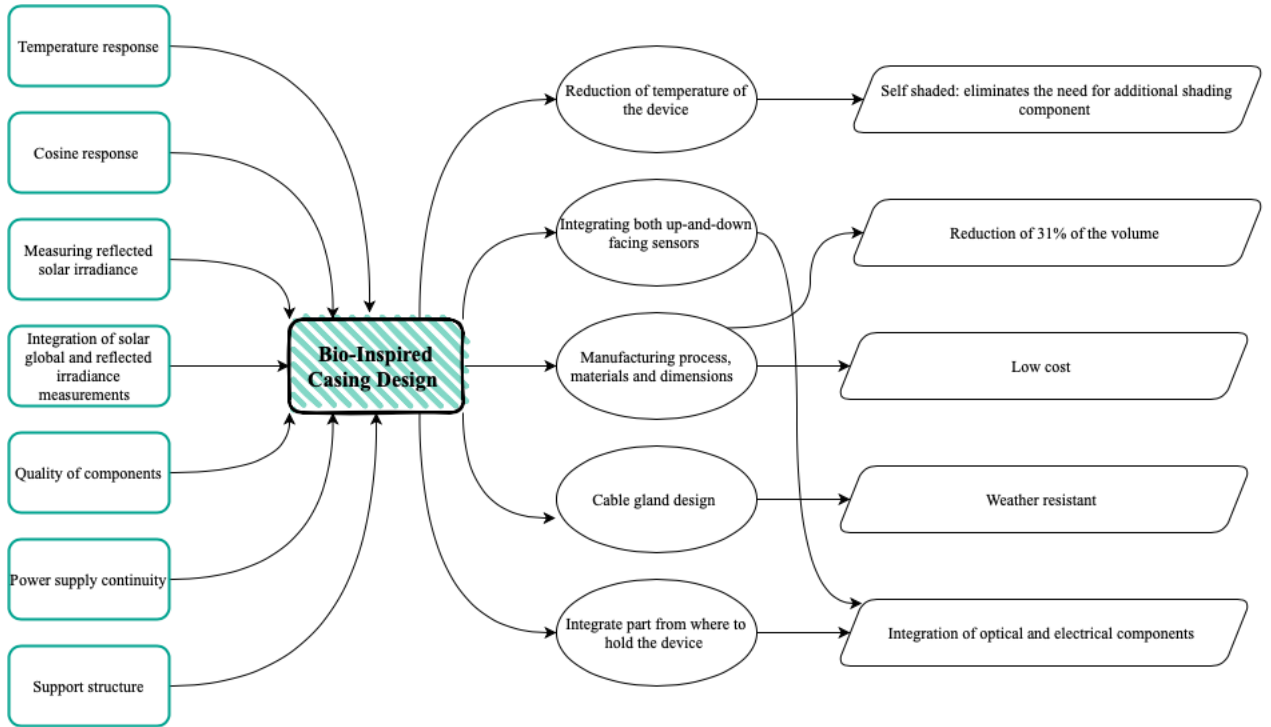
Figure 11: Relation between design requirements and casing design main improvements

The casing went through several changes during the design process. These changes were based on temperature experiments realized with different configurations of the casing. Since the design is inspired in the thermal convective and self-shading properties of cacti, temperature testing aimed to find the best configuration that incorporated this element without sacrifice other properties of the sensor, such as its resistance to weather. During the temperature tests, the temperature increments during the operation of the device were compared for several variations of the casing design. The configuration with the least temperature increments was considered the best. Three rounds of temperature tests were done before selecting the final version.
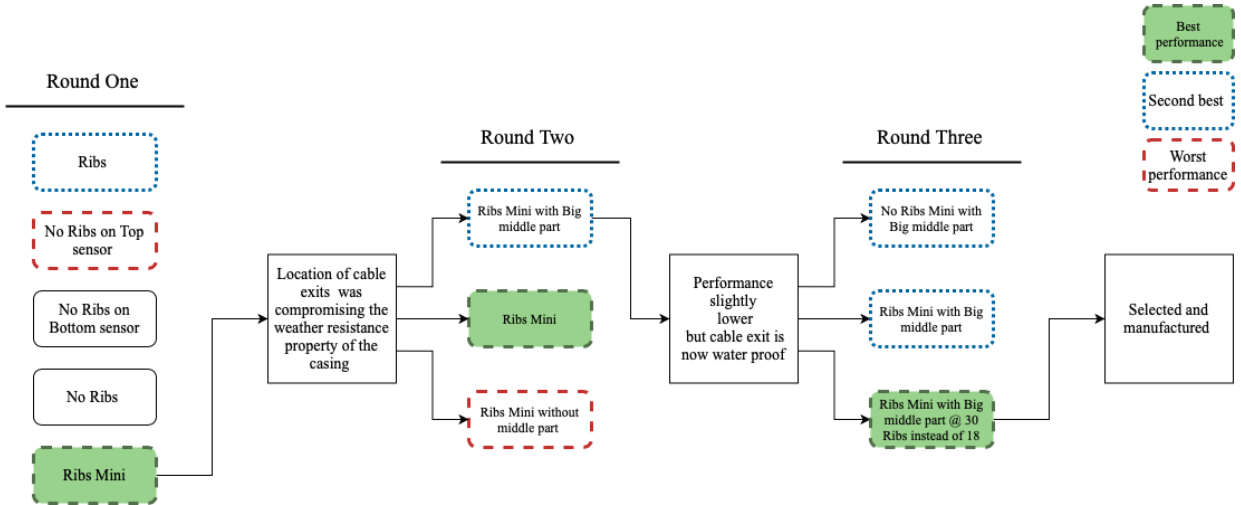
Figure 12: Temperature experiments overall results per round.

During the first round, five configurations were tested. The design with the smallest temperature increment was the casing with 18 ribs and a smaller diameter "Ribs Mini". Nevertheless, it was concluded that the design compromised the weather resistance of the instrument. The second round of tests aimed to solve this problem by proposing two configurations in which the cable exit was not in the junction of the components. None of the proposed solutions had better performance in terms of temperature, but the second-best was selected to guarantee the device is waterproof. Finally, the third round of tests was made comparing the previously selected casing. In the final round, the aim was to evaluate whether eliminating the ribs or increasing them would improve the performance of the design. It was found that increasing the number of ribs improved the design considerably. Consequently, the final design of the casing has 30 ribs, 12 more than the original design. Figure 12 summarizes this process.

Final prototype.

Due to the geometry complexity, the cheapest and fastest manufacturing solution was Direct Metal Laser Sintering (DMLS) 3D printing. Aluminium was the selected material due to its good thermal properties, low weight, and high corrosion resistance. AlSi10Mg is the Aluminium casting alloy usually used in DMLS and is consequently the final material of the device. Since the instrument needed to be weather resistant silicon sealants between the casing junctions were added (see Figure 16). An in-house silicon cable gland was fabricated to avoid dust and water entering the sensor (see Figure 13).
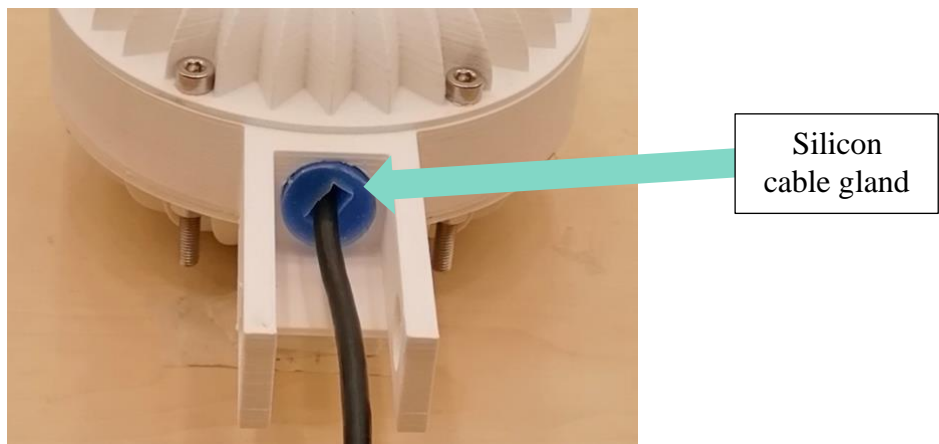
*Figure 13: In-house designed silicon cable gland*

Additionally, a silica gel desiccant was left inside the device to avoid the formation of water inside the device. A spirit level (see Figure 16) was attached to the casing to indicate whether the sensor is level. All components were mechanically assembled with screws except for the diffuser which was glued. The new design represents a reduction of 31% of the volume compared to the previous version.
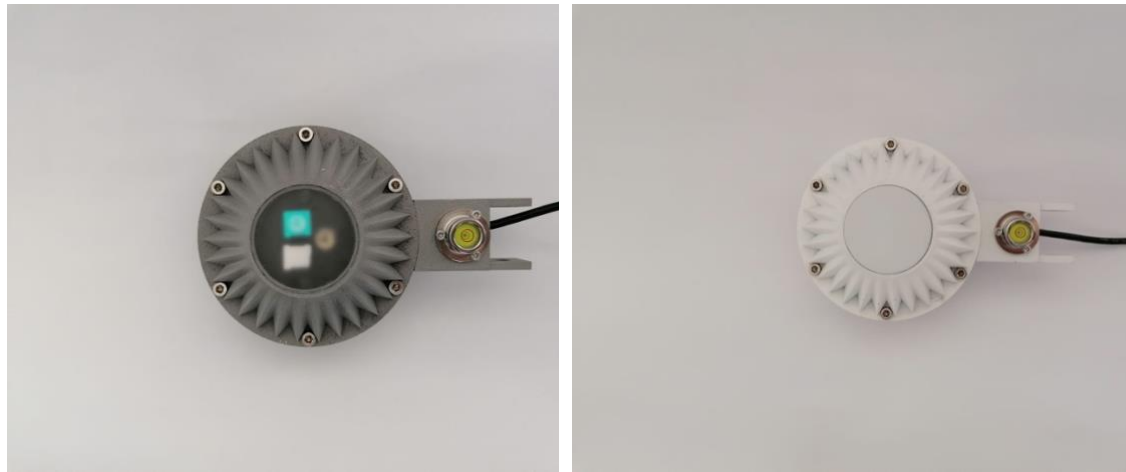
Figure 14: Grey albedometer with N-BK7 Ground Glass Diffuser

Figure 15: White albedometer with Hybrid diffuser
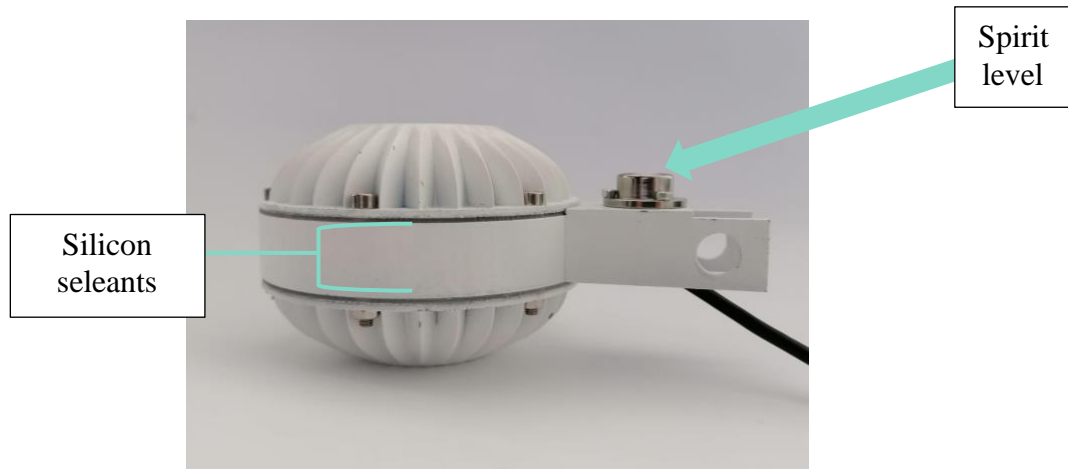
Figure 16: Side view of albedometer final prototype

As mentioned before, current technologies that measure spectral albedo are not cost-effective. For this reason, it was essential to keep the cost of the device as low as possible without compromising the accuracy of the sensor. Compared to the previous V1 pyranometer, which had a total cost of €345. The final prototype of the present albedometer represented an increase of the cost of 43%. Considering that to measure the albedo, one would need two V1 pyranometers giving a total cost of €690. Even though the cost of the device incremented considerably, the sensor is still substantially cheaper than the ones currently in the market.

Table 2: Cost of V1 solar sensor [8]

Components	Quantity	Price (€/ piece)
Photodiodes	3	9.68
Hot Mirror Optical Filter	1	103
Longpass Optical Filter	1	73.28
N-BK7 Diffuser	1	44.27
Enclosure	1	27.52
PCB	2	31.74
Other Components	-	5
TOTAL		345

Table 3: Total cost albedometer

Component	Final Cost (€)
Filters	€ 48
Diffuser	€ 43
Casing	€ 774
Spirit Level	€ 8
PCB assembly	€ 96
Other Components	€ 18
Total	€ 987

3. Optical Design

The optical design of the device aims to achieve uniformity of light reaching the sensor and provide accurate detection of irradiance across three different wavelengths using optical filters. The previous version of the sensor failed to provide sharp spectrum ranges and measured light differently depending on the position in which the sensor was placed. Solutions to this include optimizing the distance between the diffuser and photodiodes, selecting new filters and diffusers, and eliminating the shadowing inside the device.

3.1. View Factor

For the optical design of a solar sensor, one is primarily interested in the magnitude and spectral distribution of the irradiance at a certain point, rather than the geometrical aspects involved in the system that affect the optical properties of the sensor [11]. However, it is convenient to separate the spectral variations from the geometrical properties since the geometry does not change. The view factor represents the geometrical properties related to the magnitude of irradiance, it remains constant, and attention can be taken later on the spectral variations and other variable properties [11]. Since the View factor directly

affects the amount of radiance reaching the sensors, it is optimal to have a view factor the closest to 1 as possible.

The view factor is the fraction of total uniform diffuse radiation transferred from a radiating area to a receiving surface [11]. In this section, the view factor would be represented with the symbol F_{1-2} indicating the flux transfer from the radiating area (Φ_1) to the illuminated surface (Φ_2). The view factor can be estimated by dividing the flux (radiation) on the illuminated area by the total flux (radiation) emitted by the radiating area:

$$F_{1-2} = \frac{\Phi_2}{\Phi_1}$$

(2)

View factors for several geometries are already derivate. Both the diffuser and the sensing area are approximated to finite circular areas with different sizes parallel to each other (See Figure 17). It is also assumed that the enclosure of the geometry is an isothermal black surface. Meaning there is only diffuse radiation and no reflected radiation. These assumptions are part of the view factor model. The view factor for parallel circular disks with their centre along the same normal is derived from (2) as:
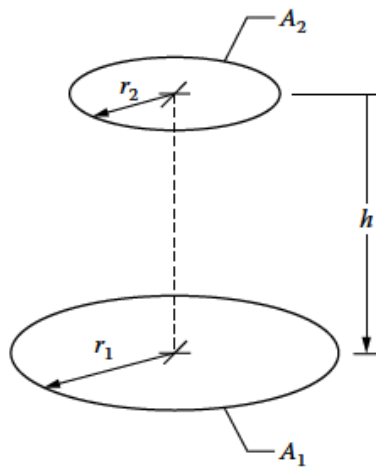

Figure 17: Parallel disk with centres along the same axis [12]

$$F_{1-2} = \frac{1}{2}\left[X - \sqrt{X^2 - 4\left(\frac{R_2}{R_1}\right)^2}\right] \tag{3}$$

Where:

$$X = 1 + \frac{1 + R_2^2}{R_1^2} \tag{4}$$

$$R_1 = \frac{r_1}{h}; \; R_2 = \frac{r_2}{h} \tag{5}$$

From this formula, the view factor between the sensing area and the diffuser was calculated and plotted for different distances between both areas to obtain the distance for which the irradiance will be measured more accurately, the following was obtained:
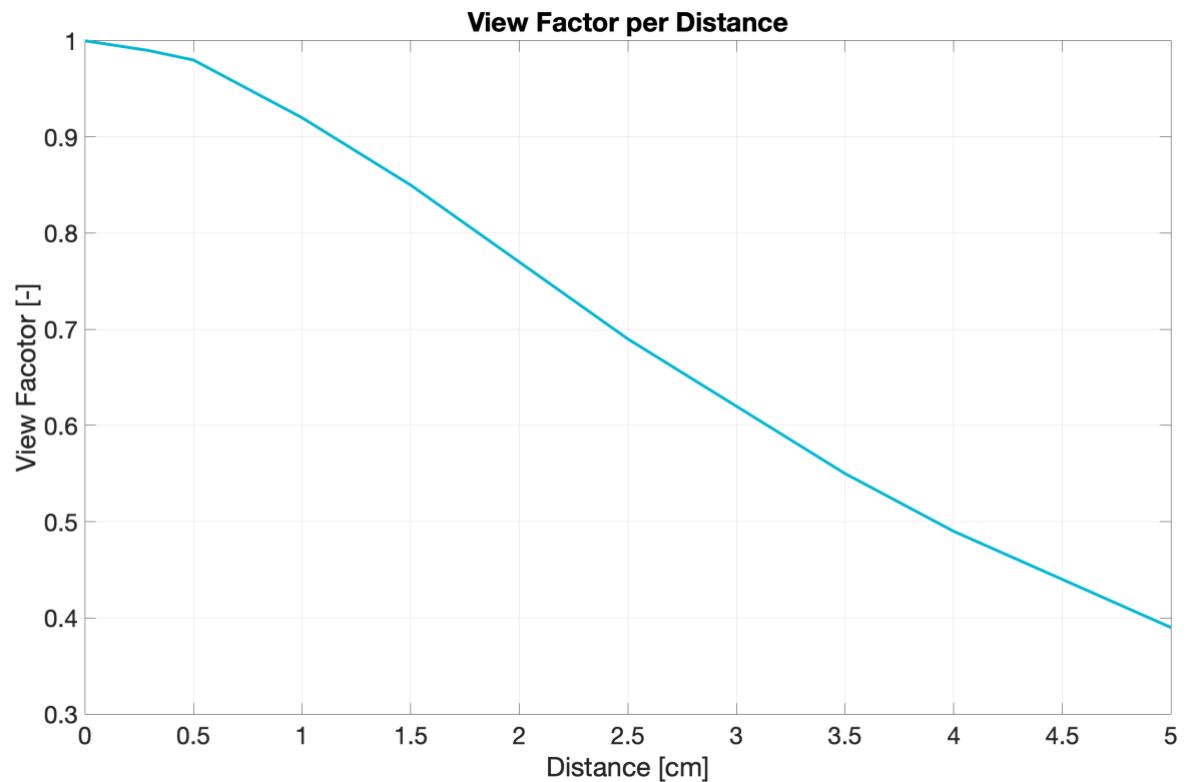

Figure 18: View Factor per Distance between the diffuser and the photodiodes

The sensing element should be as close to the diffuser as possible to obtain a view factor close to 1, as shown in Figure 18. The view factor can be used to correct the measurements obtained if the casing design or other elements do not allow the implementation of an optimal distance. However, one should still aim to reduce it as much as possible to avoid other error sources such as the ones produced by the optical properties of the diffuser in terms of angular response. Other errors caused by different optical properties will be explained in more detail later in this Chapter. The achieved view factor after optical, electrical, and mechanical considerations is 99.3%. The 0.7% missing will be considered for the calibration of the device in Section 6.1.

Enclosure

From the previous calculation, between the diffuser and the sensing elements, an optimal distance of 2.9 mm (7mm from the diffuser to the PCB) was implemented. With a view factor of 99.3%. To ensure that this distance is always guaranteed, a cylinder enclosure for the printed circuit board (PCB) was 3D printed. The enclosure creates a wall surrounding the PCB and absorbs the incoming light that does not reach the sensors. Since during the calculations of the view factor, it was assumed to be no reflected irradiance inside of the device, the material was set to be black PLA. The low reflectivity of black aims to reduce any reflectance inside the sensor.
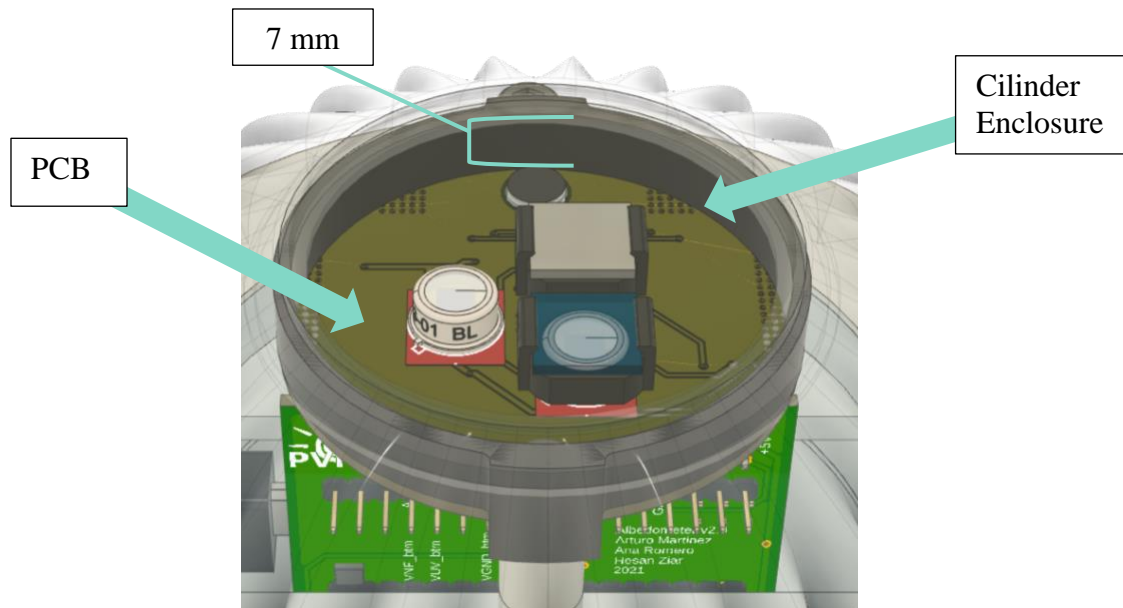
Figure 19: PCB Enclosure, the enclosure keeps the optimal distance between the photodiodes and the diffuser and reduces reflectivity inside of the device

3.2.   Shadowing

The previous version of the irradiance sensor (V1) presented inconsistencies while measuring light entering the device from different angles (azimuth). The angles with a more significant deviation corresponded to an azimuth between 75º to 175 º. This problem increases at more prominent angles of incidence. Consequently, experiments were carried on identifying the origin of the problem. The following graphs are an example of the obtained results. Both graphs represent the same angle of incidence (45°) and the same radiation source. The x-axis represents the side from which the light enters the device (azimuth), and the y-axis shows the current measured by the photodiodes.
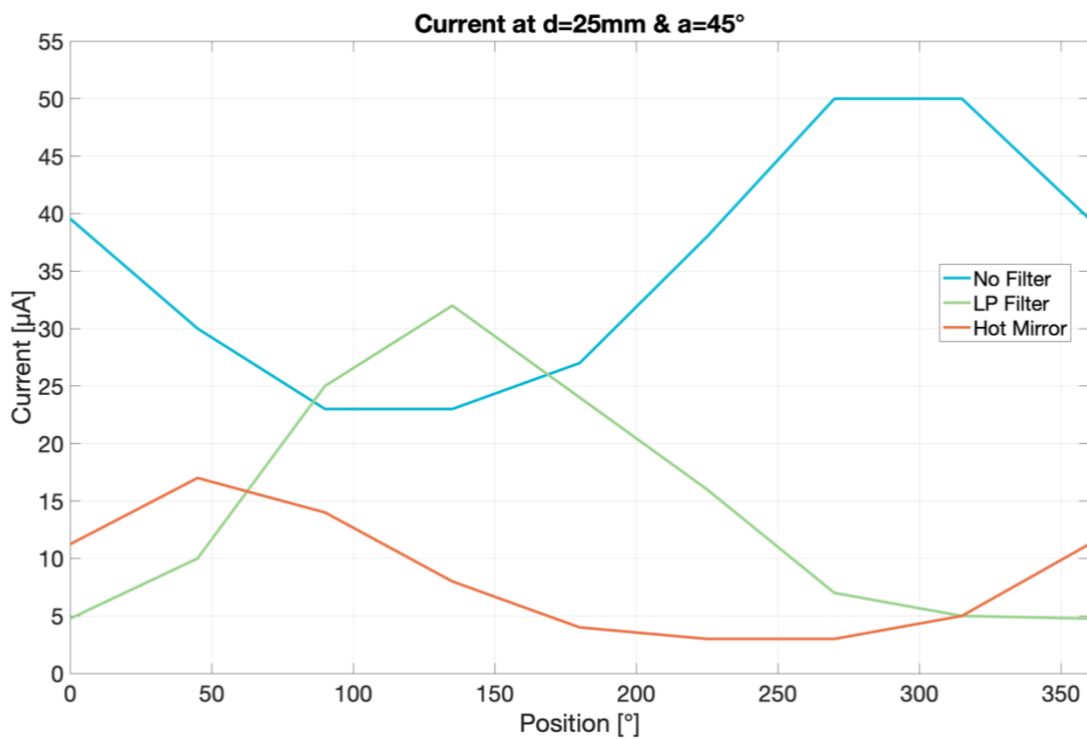

Figure 20:Photodiode current measured by V1 at a distance of 25mm and an angle of incidence of 45°
for different positions (azimuth angles)

The results for the V1's distance between the diffuser and the PCB (25mm) are shown in Figure 20. There, one can observe that at a position between 180 and 90 degrees, the no filter sensing element (320-1100nm), which is supposed to measure the highest current, measures lower values than the diode measuring between 850 to 1100 nm (LP Filter). Additionally, in some positions, the sensing elements with filters do not measure any current at all. The reason for this is because, in those orientations, the photodiodes are shadowed by the casing and the filters and the fact that the diffuser is not Lambertian, limiting the uniform diffusion of the previous version to a 10° - 20° scattering angle from the peak [8], this shadowing effect can be seen in Figure 22.
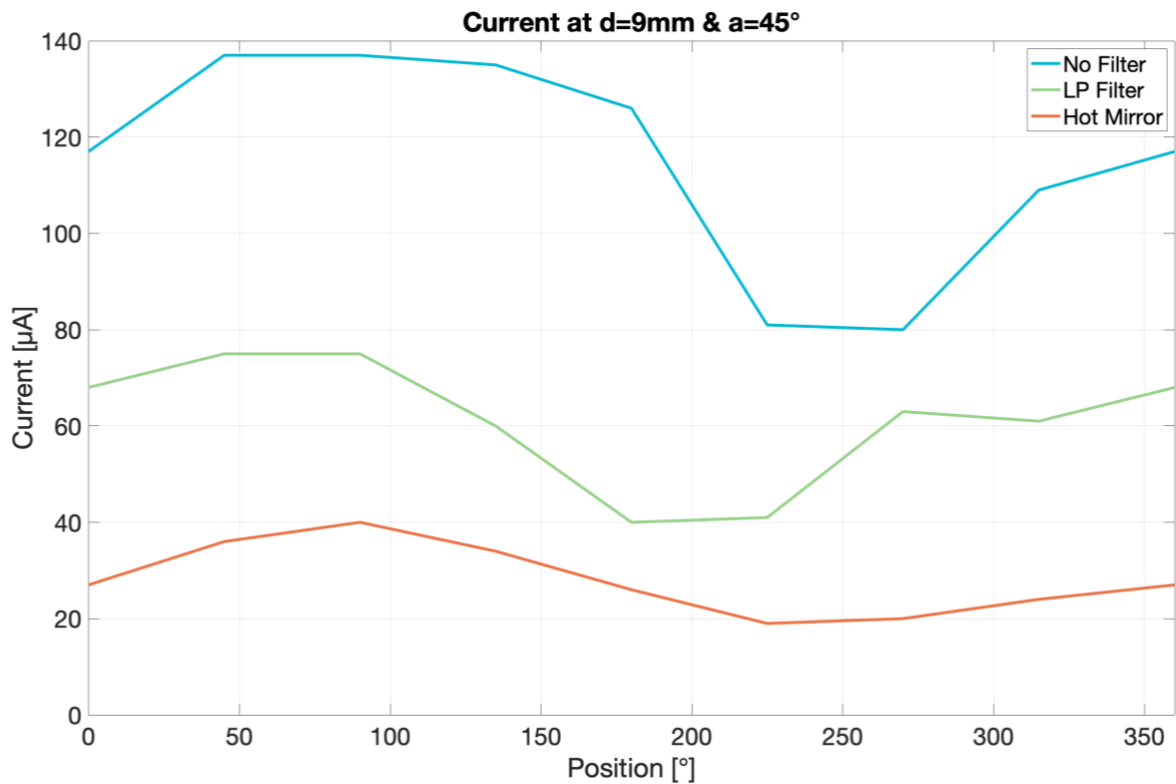

Figure 21: Current at d=9mm & a=45, where d is the distance and a is the azimuthal angle from which the light enters the device

One can compare in Figure 21 that this effect is eliminated by reducing the distance between the diffuser and the diodes. For these experiments, the distance was reduced to 9mm. One can also observe that the device measured more radiation at a

shorter distance, with a maximum current of 140 µA for the no-filter diode compared to 50 µA in the original design. From these calculations, the previous maximum angle of incidence was improved from 30° to 80°. Consequently, the new sensor detects irradiance without shadowing at increasing angles.
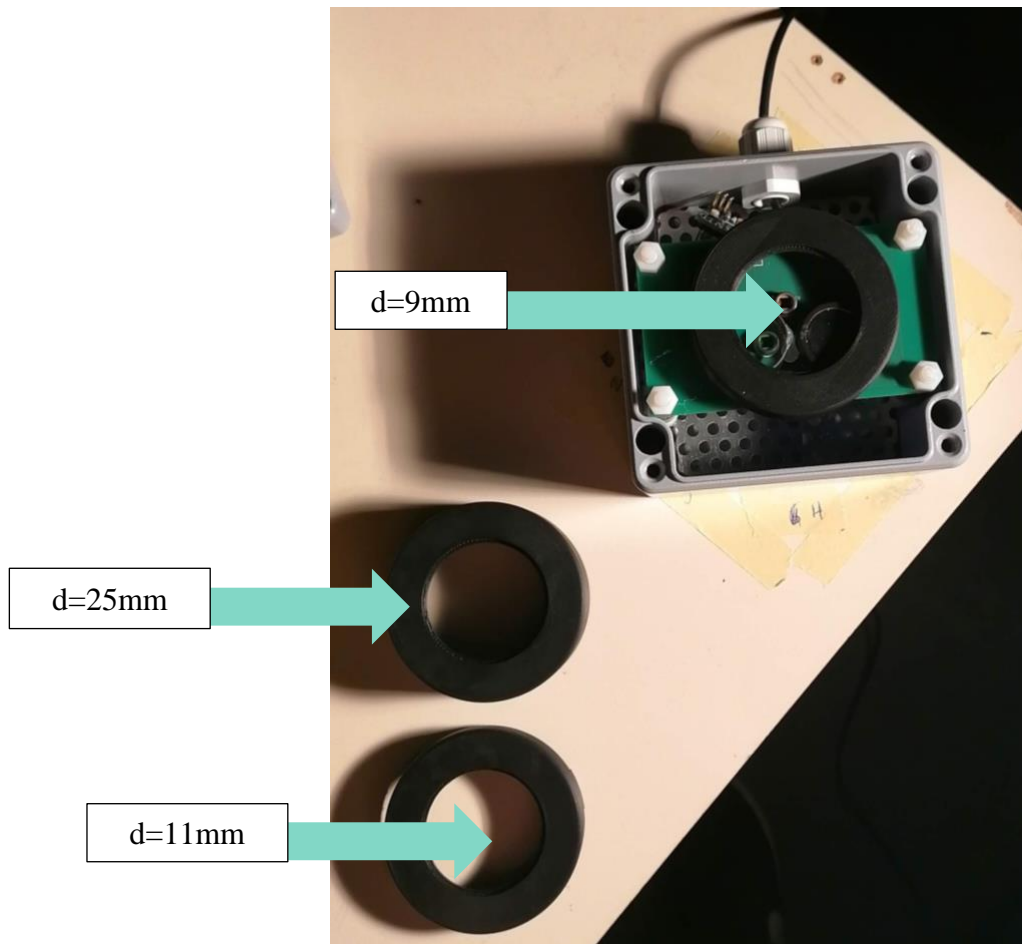
Figure 22: Shadowing produced by the casing at different distances between the diffuser and the PCB

As mentioned in the previous section, the new version will have a distance of 2.9 mm from the photodiodes to the diffuser (7mm from the diffuser to the PCB). The reason it was possible to reduce the distance even more because than what was measured in these experiments relies on the new selection of filters, which will be explained in the following section.

3.3. Optical Filters

The following modification was regarding the filters used to separate the spectrum. The first sensor version has one hot mirror (HM), one long-pass (LP) filter, and a photodiode with no filter at all. The idea was to create two ranges measured by the filtered diodes, and the third range was estimated by subtracting the current measured by the filtered diodes from the no filter diode. However, this arrangement does not consider the current measured between 320 and 360 nm (Figure 23). Of course, this is not ideal because that current is currently added to the current between 690 - 850 nm, decreasing the device's accuracy.
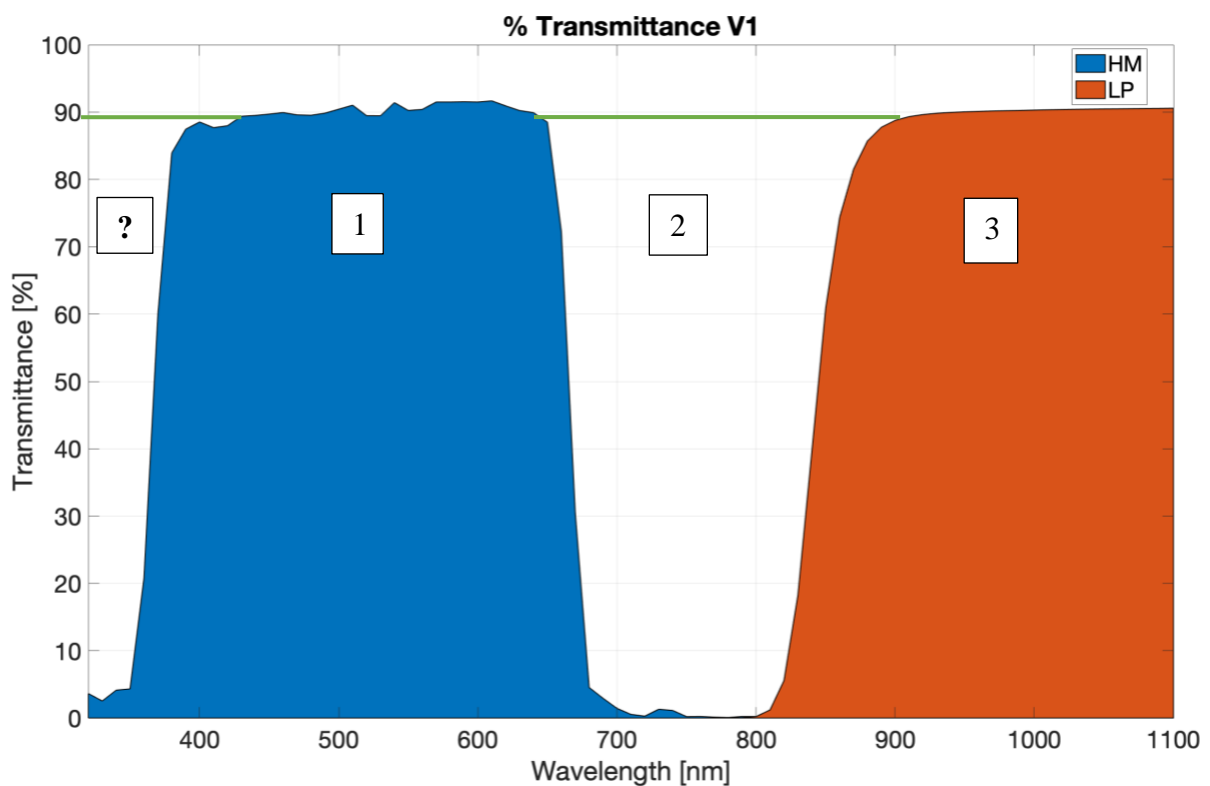

Figure 23: Transmittance percentage of V1 optical filters showing how spectrum is divided by the filters

After analysing different bandpass filters and long-pass filters that could eliminate this problem, it was concluded that this could be solved by using two long pass filters instead of a bandpass and a long pass. "20CGA-590" transmits light between 590-1100nm and "20CGA-850" transmits light from 850-1100nm.

By doing this, the sensor will have three sharp wavelength ranges, and the problem is eliminated (Figure 24). Additionally, these new filters will make it possible for future versions to select from up to 20 different cut-on wavelengths that are available if desired. They represent a reduction of 86% of the cost of the filters compared to the previous design.
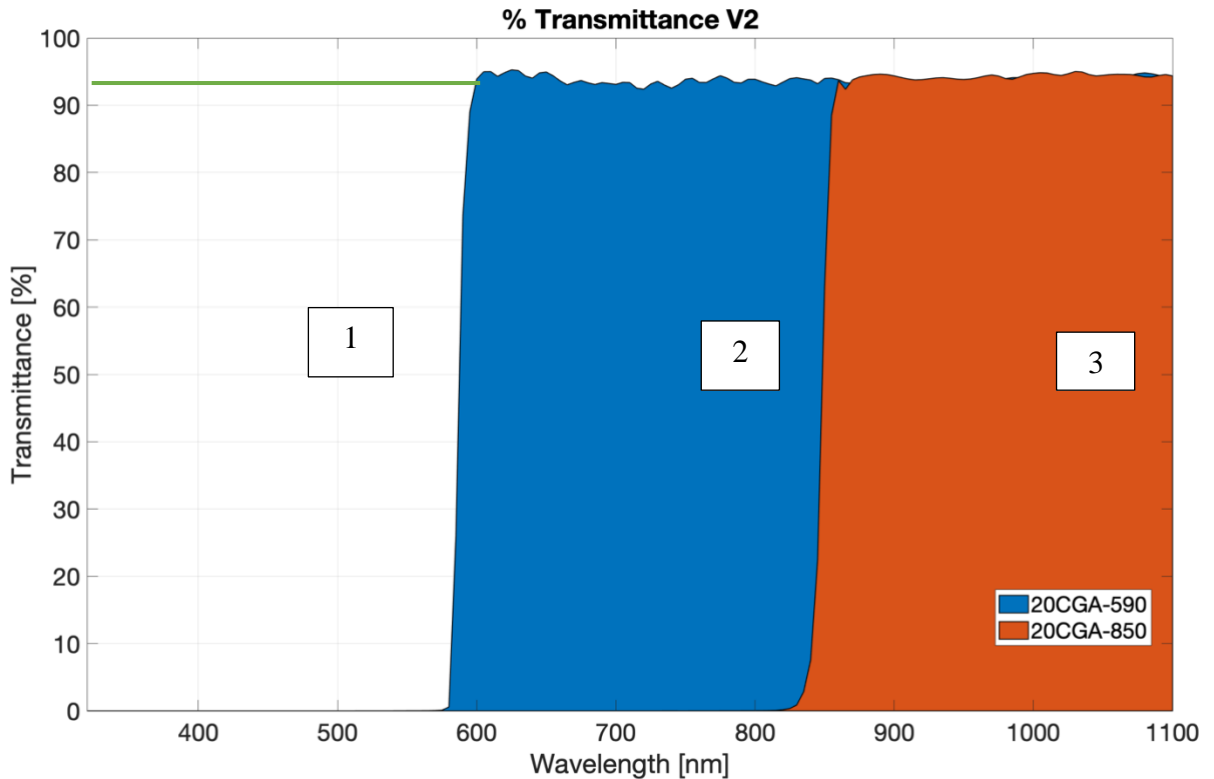

Figure 24: Transmittance of new filters showing how spectrum is divided by the filters

Filter Holders

In addition to the sharper spectrum ranges, the new filter allowed me to reduce the size of the filters and consequently the PCB size and distance between the photodiodes. The importance of this is explained in the previous chapter. Nevertheless, reducing the size of the filters made it complicated to assemble them as before (glued). Consequently, I designed filter holders that hold to the photodiodes and keep the filters in place even in the down-facing sensor. Additionally, to make the design more visually appealing, it reduces the shadow that bigger filters produced in the neighbour photodiodes and reduced the wasted material of having filters that doubled the size of the diodes.

Figure 25: Filter holder and optical filter
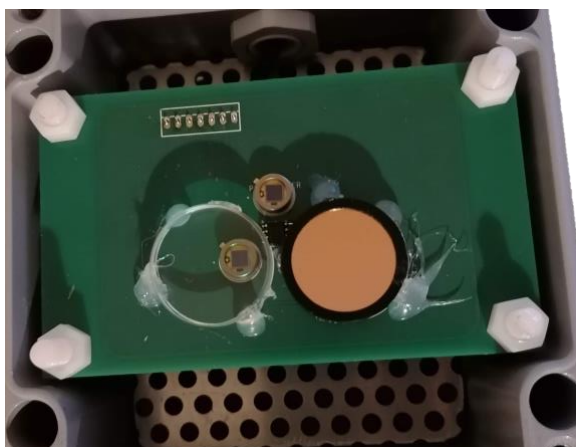
Figure 26: V1 PCB Filter Assembly
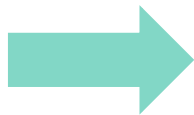
Figure 27: New PCB Filter Assembly showing how the filter holders attach the filters to the photodiodes

3.4. Diffuser

As mentioned before, the uniformity of light reaching the sensors and a good cosine response are priority design requirements. A new diffuser was selected, aiming to improve these properties more. The graph below compares the diffusers' transmittance

percentage of the old diffuser (N-BK7) and three different options. The desired diffuser must have high constant transmittance, as well as good scattering properties.
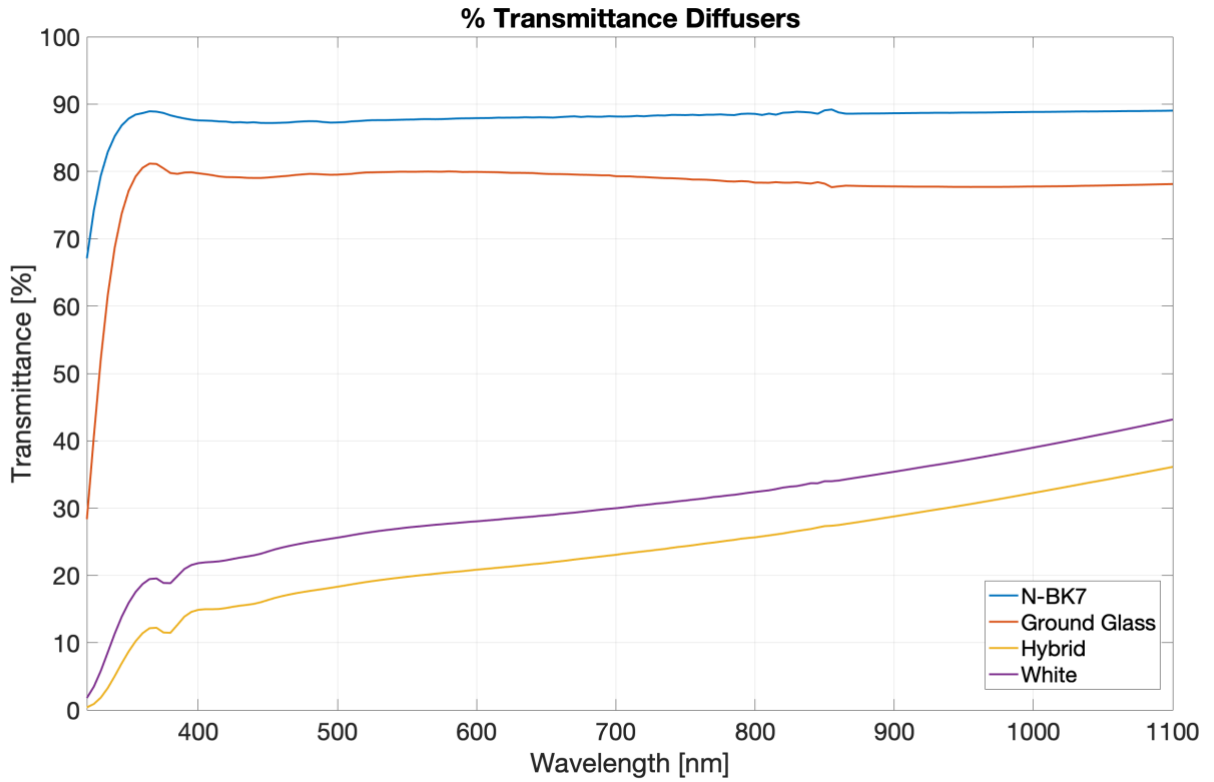

Figure 28: Comparison of old diffuser's transmittance to ground glass, hybrid, and white diffusers

The previous diffuser was selected due to its high transmittance (>80%). From the transmittance comparison, the old diffuser has the best performance. However, at higher wavelengths, its scattering properties are poor, affecting the device's accuracy for near-infrared light [8]. The scattering properties were supposed to be measured using ARTA. However, due to equipment issues, the new diffuser was chosen based on the product specifications. Ground Glass Sandblasted diffuser was not further considered due to its similar scattering properties as the N-BKT with lower transmittance.
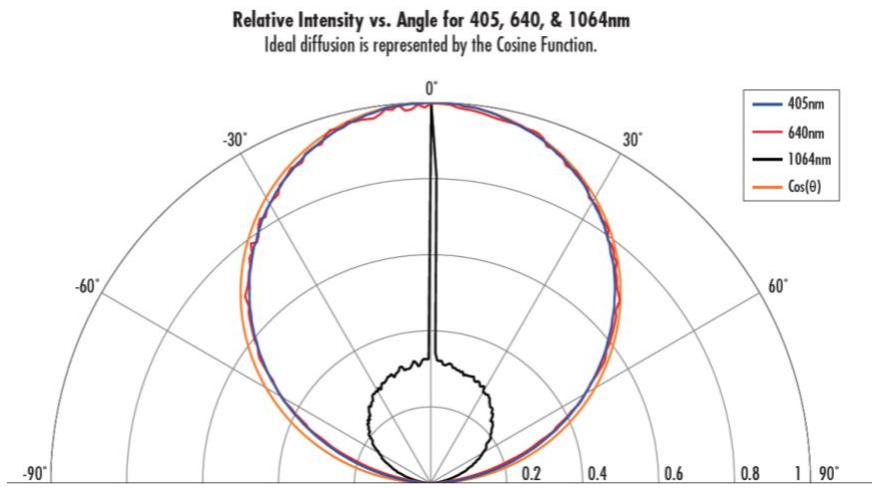
*Figure 29: White diffuser relative intensity per angle* [13]
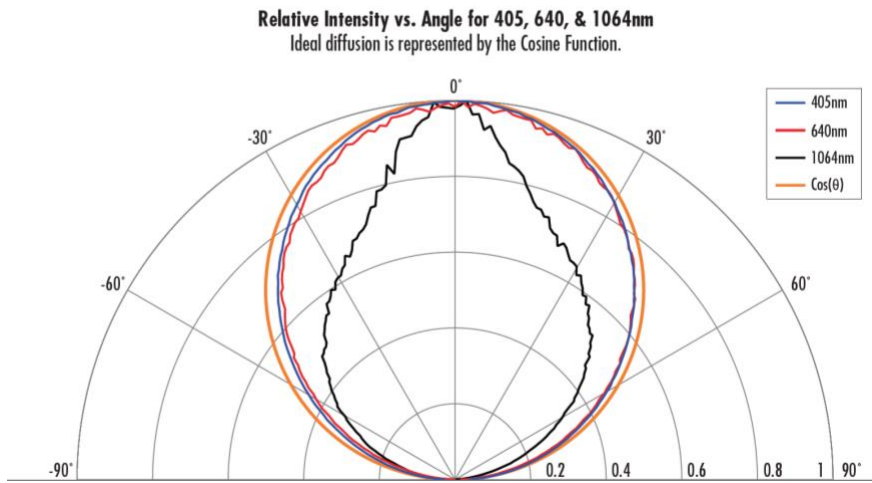
*Figure 30: Hybrid diffuser relative intensity per angle* [14]
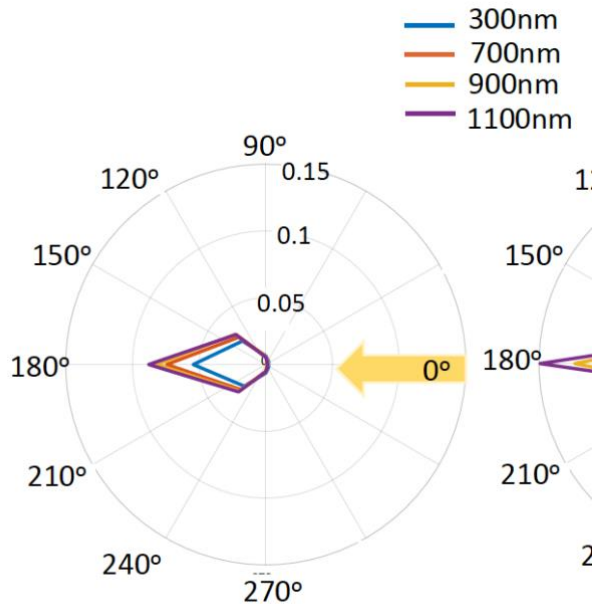
Figure 31: N-BKT diffuser relative intensity per angle [8]

Even though the hybrid diffuser presents the lowest transmittance, it was chosen over the white diffuser due to its better angular response at higher wavelengths. It has near Lambertian characteristics, which implies that the diffusion of light will be independent of the angle of incidence; This is required for the sensor to guarantee that independently from the position of the sun, the light will be diffused evenly inside the device and will be measured equally by the sensors.

However, due to the very low transmittance of this diffuser, there were still concerns about its performance since the minimal irradiance measured by the sensor will be reduced. Therefore, it was decided that both the N-BKT and Hybrid diffuser will be installed on two separate sensors. The N-BKT will be installed in a grey sensor and the Hybrid diffuser in a white sensor. The performance of each diffuser will be further analysed in Chapters 6 and 7.

4. Electrical Design

The electrical design of the albedometer correlates with several function requirements established in Chapter 1.3. It contains the sensing elements which provide the irradiance measurements, influences the casing design, and secures power supply continuity and data collection. The main changes in the electrical design, compared to V1, were the dimensions, colour and assembly of PCB and the data collection that now integrates both global and reflected solar radiation measurements collected from the up-and down-facing sensors.

Printed Circuit Board Assembly

The printed circuit board assembly is the leading electrical component of the sensor since it connects and supports most electrical components. All PCBs were designed and assembled by Arturo Martinez Lopez integrating both optical and mechanical improvements of the device. The first modification reducing the sensing PCB area from 66.78 cm^2 to 19.63 cm^2 which made it possible to downsize the casing and modify its geometry. The main components of the new PCB assembly are shown in Figure 32 and they can be compared to the PCB assembly of V1 in Figure 4. Secondly, a second sensing PCB was added to have both up-and-down facing sensing measurements needed for measuring the albedo. Third, both sensing PCBs were attached to a third PCB, which integrates global and reflected solar radiation measurements into a microcontroller board (Arduino Micro). Finally, the colour of the sensing PCB was changed from green to black. It aims at reducing the reflectance of light from the surface of the PCB to the photodiodes.
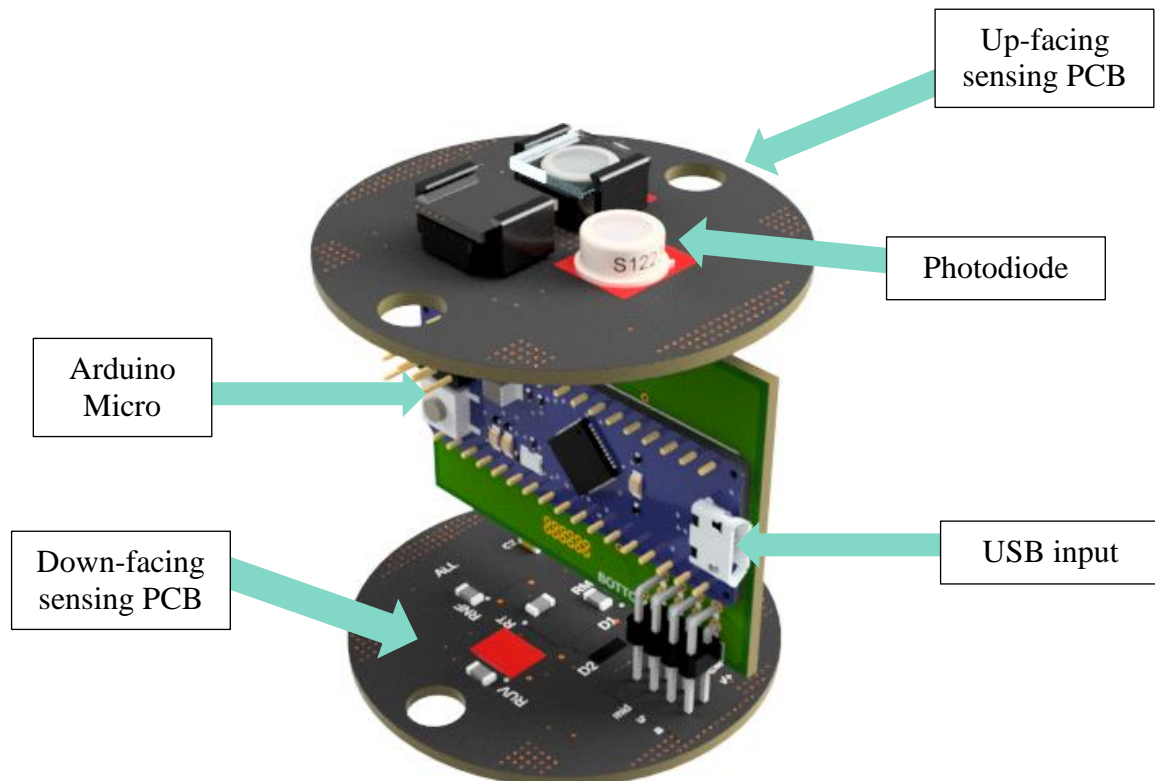

Figure 32: PCB Assembly main components

Photodiodes as Sensing elements

Silicon Photodiodes are semiconductor devices that detect light from near ultra-violet to the infrared spectral regions, making them ideal for this application. Three silicon photodiodes were used to measure the three different solar spectrums in each sensing PCB. Below are some of the main characteristics of photodiodes.

Table 4: S1223 Photodiode Parameters

Parameter	Symbol	Condition	Value	Unit
Spectral Response Range	λ	-	320-1100	nm
Photosensitivity	S	λ_{peak} / 660nm / 780nm / 830nm	0.6 / 0.45 / 0.52 / 0.54	A/W
Noise Equivalent Power	NEP	VR=20 @ λ_{peak}	9.4 E-15	$W/Hz^{1/2}$
Dark Current	I_D	VR= 20V	0.2	μA
Effective area size	A	-	6.6	mm^2
Temperature Coefficient	T_{CID}	-	1.15	Times ºC

Data collection

The current values measured by the photodiodes in both up-facing and down-facing sensing PCB are integrated into a microcontroller board. The microcontroller is connected to a Raspberry Pi through a USB-Ethernet-USB cable connection. In the Raspberry Pi, data is stored. Current collected data will be later translated to Irradiance during the device's calibration, considering the photodiodes parameters shown in Table 4. The main problem for data collection was the compatibility of the USB cable that exits the device with the waterproof requirement in the casing design. The waterproof requirement was solved by designing and fabricating a silicon cable gland that fitted both the casing and adjusts to the cable geometry (see Figure 13).

5. Mechanical Design

The mechanical design aims to integrate both optical and electrical designs in the sensor's casing. During the HoQ analysis, it was found that many functional requirements were strongly correlated to the casing design. Such as temperature and cosine response, integrating both global and reflected irradiance, and quality of components. A bio-inspired casing was designed to tackle these requirements.

5.1. Bio-Inspired casing design

Photodiode sensors are susceptible to temperature changes during operation. There are two main reasons why temperature should be monitored. First, the absorption spectrum shifts to longer wavelengths in silicon diodes when temperature increases [15]. Consequently, the responsivity for short wavelengths reduces (has a negative temperature coefficient). Positive temperature coefficients are present in higher wavelengths since the detector's responsivity increases at higher temperatures [15].

Additionally, dark current almost doubles for every 8 to 10 ºC, which influences the noise in the detector and the minimum detectable power. Both reasons affect the

accuracy of the measurements by this type of detector [15]. By keeping the temperature increments at a minimum or cooling the system, one can eliminate these effects.

The casing design aims to reduce the temperature effect in the sensitivity of the device; looking for different options for the casing design and taking into consideration that regulation of temperature was essential, it was concluded that one could mimic the strategy and behaviour of one of the best temperature regulators in nature: cacti. A cactus has a unique technique to survive. The main characteristic of a cactus is the ribs and spines that cover the entire plant. Spines and ribs serve to shade the plant from the harsh sun. It shades the plant to keep the internal temperature down low enough so that the water that the plant stores does not evaporate. This ability is vital for surviving in such a sweltering and arid climate. These technologies can be implemented in other designs.

Figure 33: Thermal image of cactus showing temperature differences in the surface [16]

Cacti inspire the casing design due to their temperature regulation properties. Several types of cacti are equipped with cooling ribs. Ribs on cacti shade the cactus' surface and improve heat radiation [17]. Ribs reduce surface temperature increases because the convective heat loss increases [18]. Comparisons between ribbed cactus and non-ribbed cactus have been made in terms of increased surface temperature. The absence of ribs represents a 1 to 2 °C rise due to the decrease in heat convection [18].
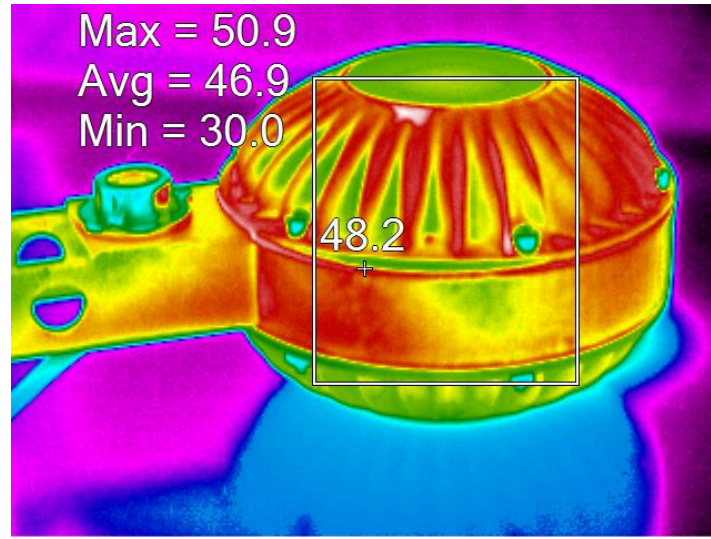
Figure 34: Thermal image of the casing design showing the same behaviour as the cactus

The casing aimed to mimic the geometry of the cactus by adding symmetrical triangular ribs around the whole surface. The number of ribs and the ratio between the depth of the ribs and the internal radius were maximized since it has been proven that having a large number of ribs crowded around a relatively narrow steam would shade each other [19]. The infrared image in Figure 33 shows how the cactus ribs have different surface temperatures due to self-shading and cooling properties. The same can be seen in Figure 34 with the ribs in the bio-inspired casing design.

5.2. Temperature tests

As mentioned before, the casing design is inspired by cacti. It is based on the statement that ribs reduce surface temperature increments because of increased convective heat loss due to these plants' ridge and furrow design. Since the ridges are more exposed to wind currents during the day, more significant heat loss is expected. From this, it is expected that the ribs in the new casing design will reduce the temperature within the device and improve the cooling properties. With this, the need for an additional shading component will be eliminated.
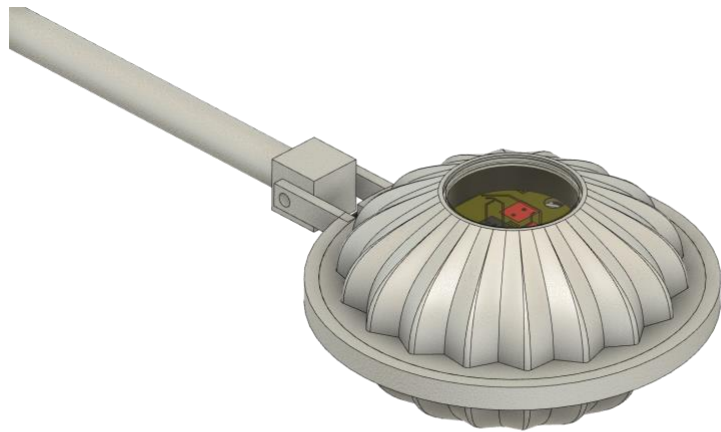
Figure 35: First version of casing design (Ribs)

To tests this, temperature experiments were carried on. For the first round of experiments, five configurations of the first casing version were 3D printed in white Polylactic acid (PLA) (Table 5). The sensors were placed for 15 minutes under a solar simulator that yields ~880 W/m^2 at three different angles of incidence (90º,60º & 30º altitude).

While the sensors were under the solar simulation, the temperature increment was recorded from the temperature sensors in both up-facing and down-facing PCBs. Later, these values were plotted for all three incident angles for both up-facing and down-facing sensors, and the temperature gradients for each configuration were estimated. The following results were obtained:

| Number	Figure	Configuration	External diameter
1		18 Ribs (Ribs)	130 mm
2		No Ribs on up facing sensor (NRT)	130 mm
3		No Ribs on down facing sensor (NRB)	130 mm
4		No Ribs (NR)	130 mm
5		18 Ribs (Mini)	105 mm
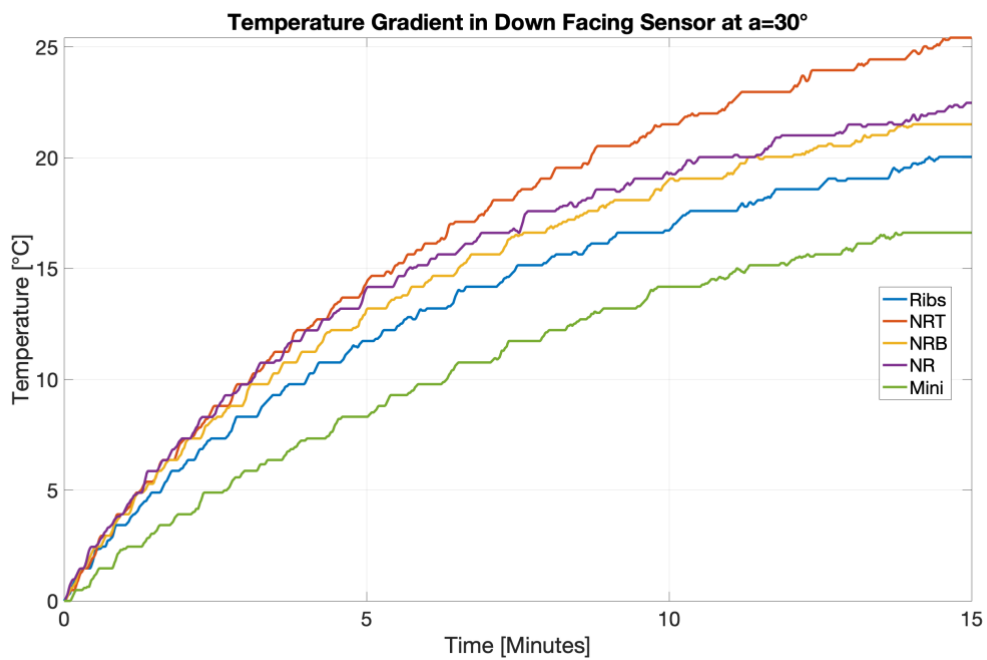
Figure 36: Temperature Gradient in Down Facing Sensor at a=30 degrees

Table 6: Average temperature Increment first round results

Configuration	Average Temperature Increment [°C/min]	Average Temperature Increment Up facing Sensor [°C/min]	Average Temperature Increment Down facing Sensor [°C/min]
Ribs	1.63	2.05	1.21
NRT	1.77	2.16	1.38
NRB	1.66	2.04	1.28
NR	1.66	2.04	1.28
Mini	**1.58**	**1.98**	**1.17**

The results showed in Figure 36 and Table 6 that the Rib configuration was better than the NRT, NRB, and NR configurations. However, the mini version of the Ribs design was considerably better than all the configurations at both up-facing and down-facing sensors. If the initial temperature is 25ºC and the operation time is 15 minutes, the mini version will operate at a temperature of 48ºC since it has a temperature gradient of 1.58

[ºC/min], 1.2ºC lower than the not ribbed version (49.9ºC) and 2.85ºC lower than the worst performer (51.55ºC)

Both Ribbed configurations showed to reduce the temperature of the sensor at 60 and 30 degrees. At an altitude of 90 degrees, all sensors performed similarly, probably due to the size of the diffuser (4.4 mm) and its high transmittance. The diffuser makes most of the light hit directly the PCB located immediately after the diffuser. Thus, at this angle, the ribs do not have much effect on the internal temperature of the sensor. From this round of tests, the Mini version was selected.

However, after looking for manufacturing processes options and other properties of the casing, it was found that it would be hard to make it waterproof. The cable output (for the cable that powers the sensor and communicates the device with a computer) was between the three parts that composed the casing (Figure 37), making it hard to seal (Figure 38).
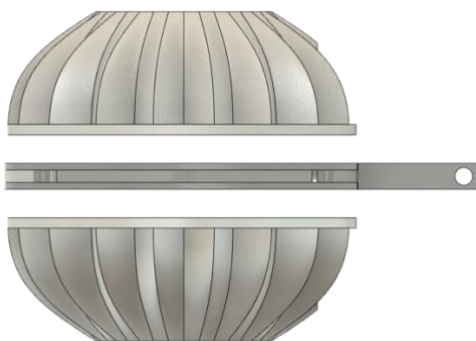
Figure 37: Mini/Original casing design consisting of three pieces: up-facing, down-facing and an intermediate piece that brings the casing together.
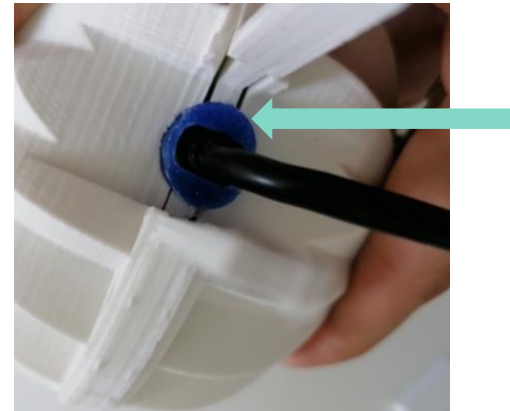
Figure 38: Sealing complications presented in the second version of the albedometer casing at the cable outlet

Because of this, two more casing configurations were designed. Where the cable output is in one part of the casing instead of three of them, temperature increment experiments were repeated with the same characteristics as before but now comparing the two new versions with the mini version previously selected. The Ribs mini version, selected on the first round, will now be referred to as "Original".
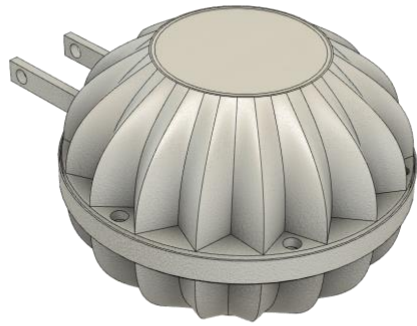
Figure 39: Second version of new casing design (Mini/Original)

Table 7: Second round casing configurations

Number	Figure	Configuration	External diameter
1		18 Ribs (Mini/Original)	105 mm
2		18 Ribs with big middle piece (Int Big)	105 mm
3		18 Ribs with no middle part (No Int)	105 mm

From this round the following results were found:
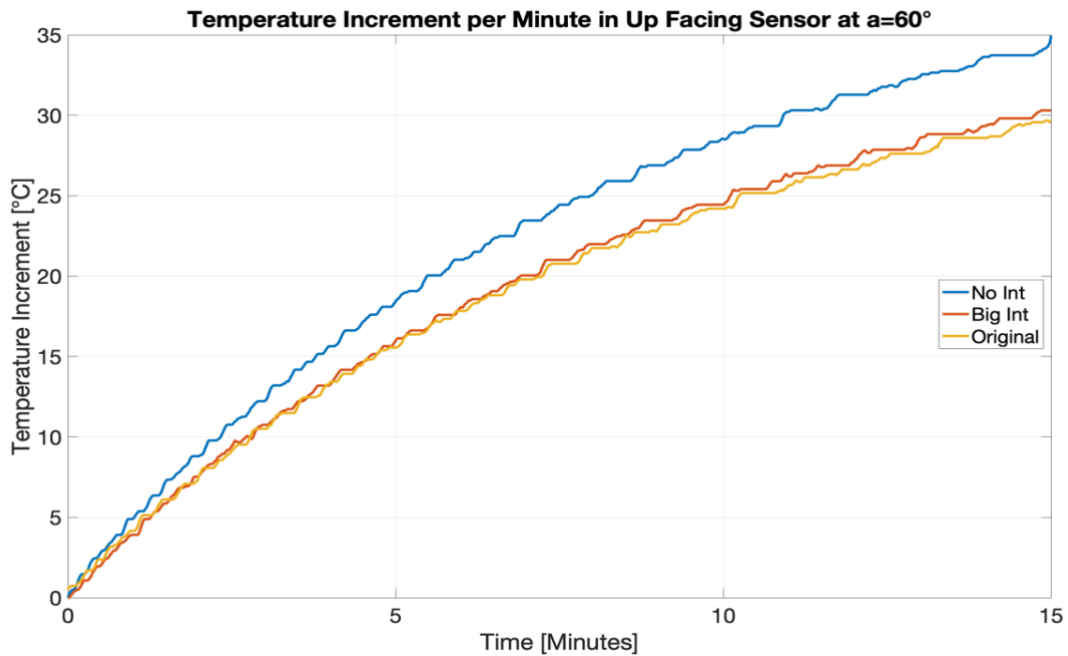
Figure 40: Temperature Increment per Minute in Up-Facing Sensor at a=60 degrees

Table 8: Average Temperature Increment results second round

Configuration	Average Temperature Increment [°C/min]	Average Temperature Increment Up facing Sensor [°C/min]	Average Temperature Increment Down facing Sensor [°C/min]
No int	1.85	2.22	1.48
Big Int	**1.70**	**2.11**	**1.29**
Original	1.62	2.01	1.22

From this round, the Big int configuration was selected. Even though the original version was still performing better, the Big Int configuration has the closest performance while eliminating the problem when making it waterproof. It is essential to mention that

even though the values in Table 8 seem higher than in Table 6, the results cannot be compared because there were made a different day with different ambient conditions.
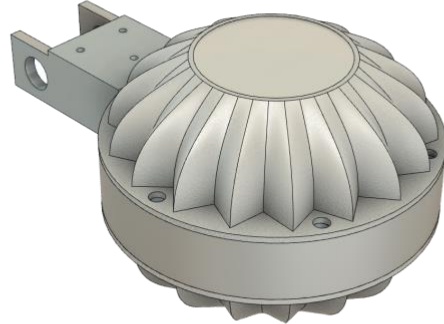
Figure 41: Third version of new casing design (Big Int)

Finally, since the geometry changed considerably, a final round with a non-ribbed version of this new design was made to confirm that the ribs in this new design have an advantage over a non-ribbed version. The significant reduction of the ribbed area consequent of the bigger intermediate part can affect the effect of the ribs. Additionally, the increase in the middle part made it possible to increment the number of ribs limited by geometrical constraints of the previous configuration. As mentioned in Section 5.1, having more ribs crowded around the same diameter potentially will increase the shading between them.

| Number	Figure	Configuration	External diameter
1		18 Ribs Big Int (Big Int 18R)	105 mm
2		No Ribs Big Int (Big Int NR)	105 mm
3		30 Ribs Big Int (Big Int 30R)	105 mm

The following results were found:
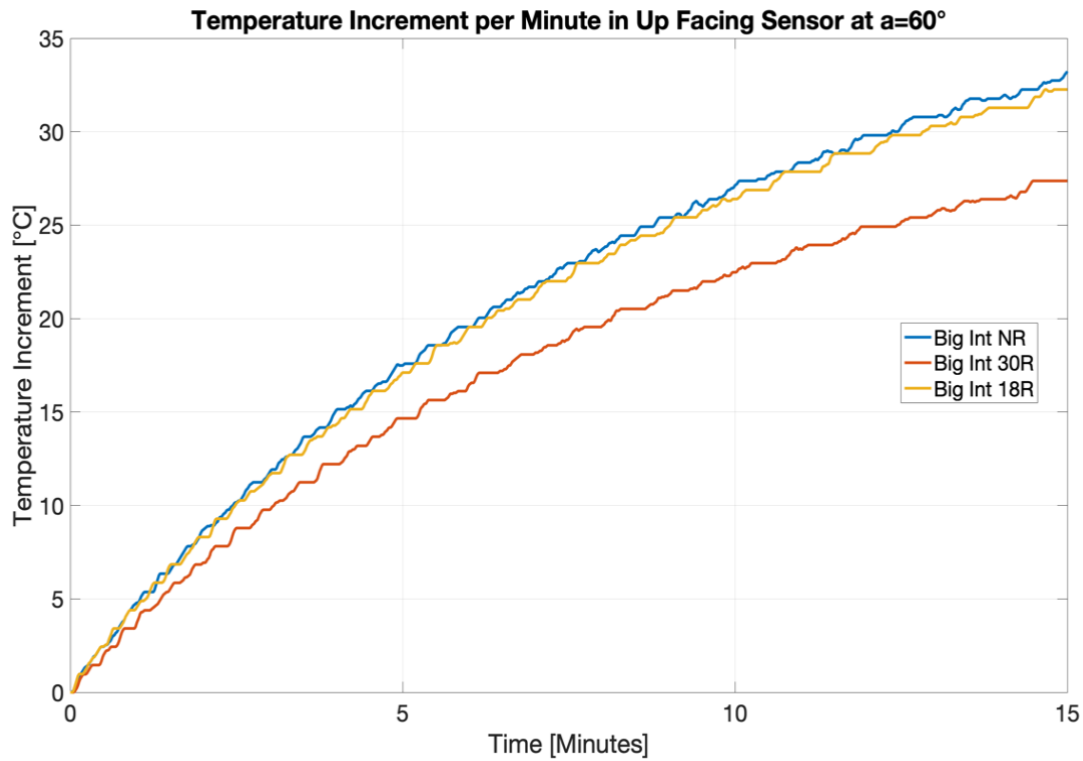
Figure 42: Temperature Increment per Minute in Up-facing Sensor at a=60 degrees

Table 10: Average temperature increment results final round

Configuration	Average Temperature Increment [°C/min]	Average Temperature Increment Up facing Sensor [°C/min]	Average Temperature Increment Down facing Sensor [°C/min]
Big Int NR	1.70	2.11	1.30
Big Int 30R	**1.52**	**1.92**	**1.12**
Big Int 18R	1.72	2.12	1.31

From the final round, it was concluded that increasing the ribs of the design reduced the temperature gradient of the sensor considerably, while the 18R and NR had very similar performance. The reduction of the 18R performance over the NR could be

since the middle part that had to be bigger has no ribs in it. It will also be ideal to have this part with ribs, but this version was not made like that due to assembly and manufacturing limitations. If operating for 15 minutes, the 30 ribs casing will represent a reduction in the sensor's temperature of 2.7ºC compared to the non-ribbed version.
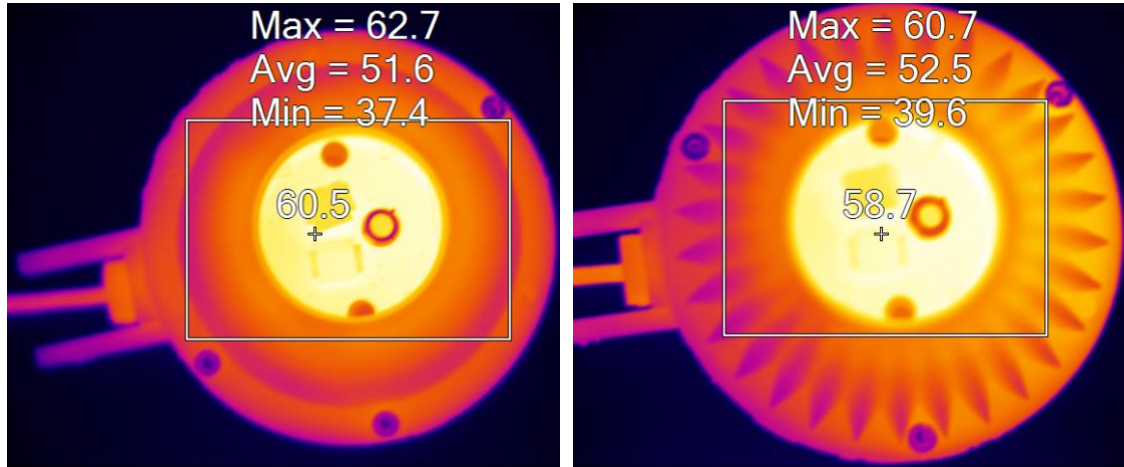
Figure 43: Thermal image of non-ribbed casing after tested at an altitude of 60º, it shows uniformity in the surface temperature at all sides of the casing

Figure 44: Thermal image of 30R casing showing how at an altitude of 60º the irradianced side (Right) has higher temperatures than the shadowed side (Left)

Additionally, pictures were taken with an infrared thermal imaging camera to compare the casing surface temperature during the previous experiments (see Figure 43 and Figure 44). The images showed that the ribs reduced the maximum temperature between one and two degrees Celsius under laboratory conditions, without wind. It also shows how the surface temperature of the ribbed casing presents lower temperatures at the side of the casing opposite to the incoming light. Finally, the final sensor's temperature gradient and cooling speed, manufactured in aluminium, was obtained. The sensor was painted white, expecting to reduce the casing temperature since white absorbs less light than darker colours. Two sensors were manufactured.

The second sensor conserved the grey colour from aluminium and will be used as a reference to determine the influence of colour in the temperature increment of the device. It is important to recall that the sensors have different diffusers; the grey sensor has an N-BKT ground glass diffuser with a percentage of transmittance <80%, while the

white sensor has a Hybrid diffuser with average transmittance >30%. It is expected that this also influences the temperature within the device, especially at higher altitudes.
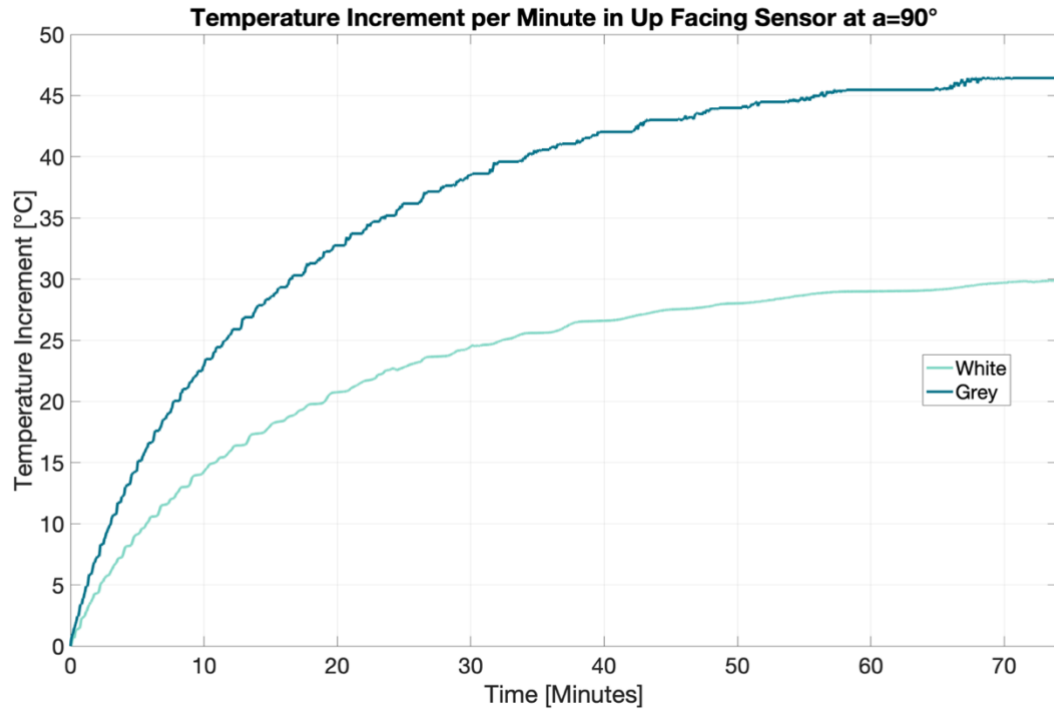
Figure 45: Temperature increment Up-facing sensor Aluminium sensors

Figure 45 shows that painting the casing white reduces the temperature increment by 20 degrees Celsius for the up-facing sensor and 10 degrees for the down-facing sensor. Both sensors were measured at the same time and under the same conditions. Thermal images of both casings also showed a difference of 8.5 degrees in average surface temperature within both colours. This can be seen in Figure 46.
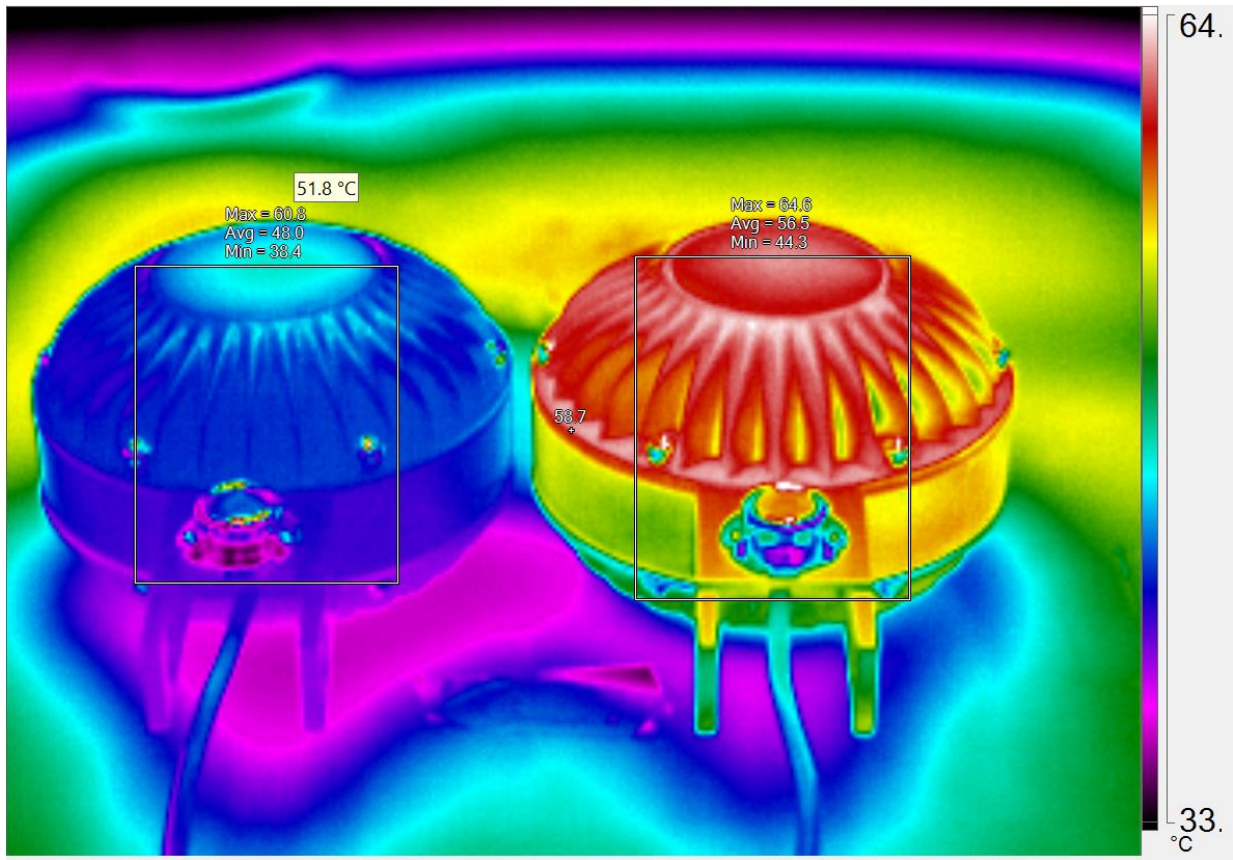
Figure 46: Thermal image of White Aluminium casing (Left) and Grey Aluminium Casing (Right)

Finally, the cooling properties of the final prototypes were measured in a closed dark room (to avoid any additional irradiance or heat source) at a constant ambient temperature of 25ºC. Both the up-facing and down-facing sensors had similar cooling behaviour in both albedometers. In Figure 47, one can see that, for the Up facing sensor, if the only heat source in the device is the power supply and electrical components, the grey albedometer takes over an hour to reach a temperature <30ºC, for the white sensor, it takes around 40 minutes to achieve so. The fact that the grey sensor reaches a temperature almost 20ºC higher has an important role in this. The grey sensors' temperatures become almost stable at around 29.8ºC (4.81ºC more than ambient temperature) while the white sensor cools down to 27.2ºC, only 2.2ºC more than ambient temperature.
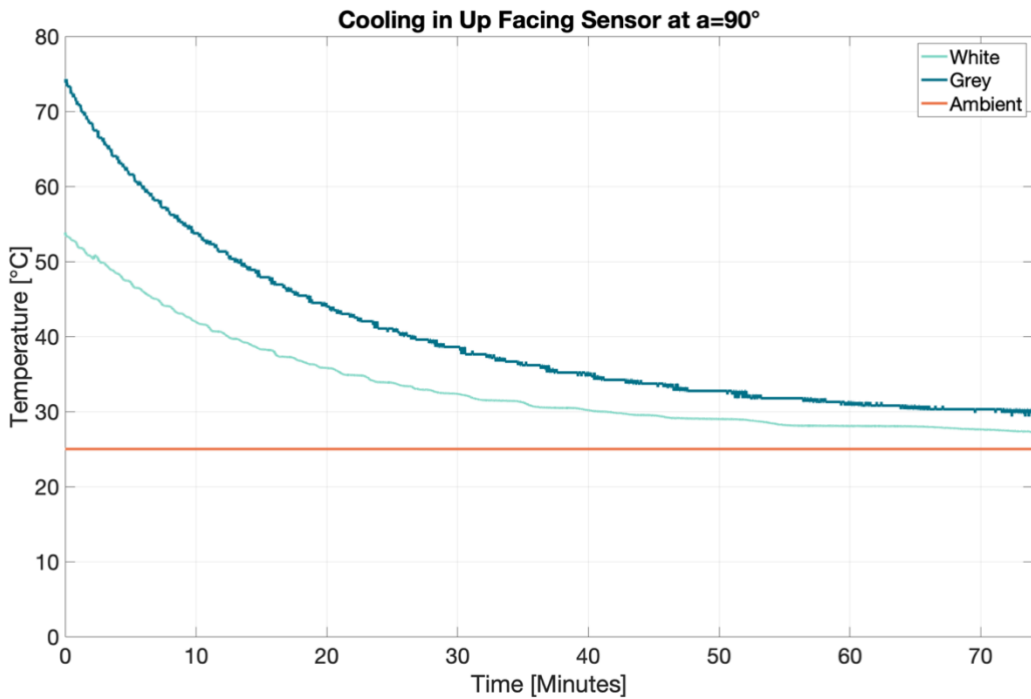
Figure 47: Cooling in Up facing sensor of grey and black albedometers at an angle of incidence of 90°. The image shows decreasing in temperature during time and the ambient temperature.

The temperature experiments presented in this section gave us insight into how the final prototype will behave in terms of temperature and how the bio-inspired design helps reduce temperature increments that could lead to changes in the photodiodes' responsivity and additional noise in the measured data. However, these experiments were done at laboratory conditions with constant irradiance, constant temperature and ignoring the effect that wind currents could have on the cooling and heating of the device. The operational temperature of the final prototypes in outdoor conditions are analysed in Section 6 and Section 7.

6. Calibration

Calibration of the instrument is essential to guarantee the accuracy of the measurements. Calibration of solar sensors can be carried out in different ways, but calibration through ASTM or ISO standards (e.g., ISO 9847 standard 'Calibration of field pyranometers by comparison to a reference pyranometer') is desired due to their worldwide acceptance. For this sensor, it was not possible to have a calibration procedure with standard conditions. However, an adapted version of the calibration procedures was done. Outdoor calibration was performed at the PV monitoring station of TU Delft. Both albedometers were attached to a Solys 2 sun tracker, rotating according to the sun's position (azimuth).
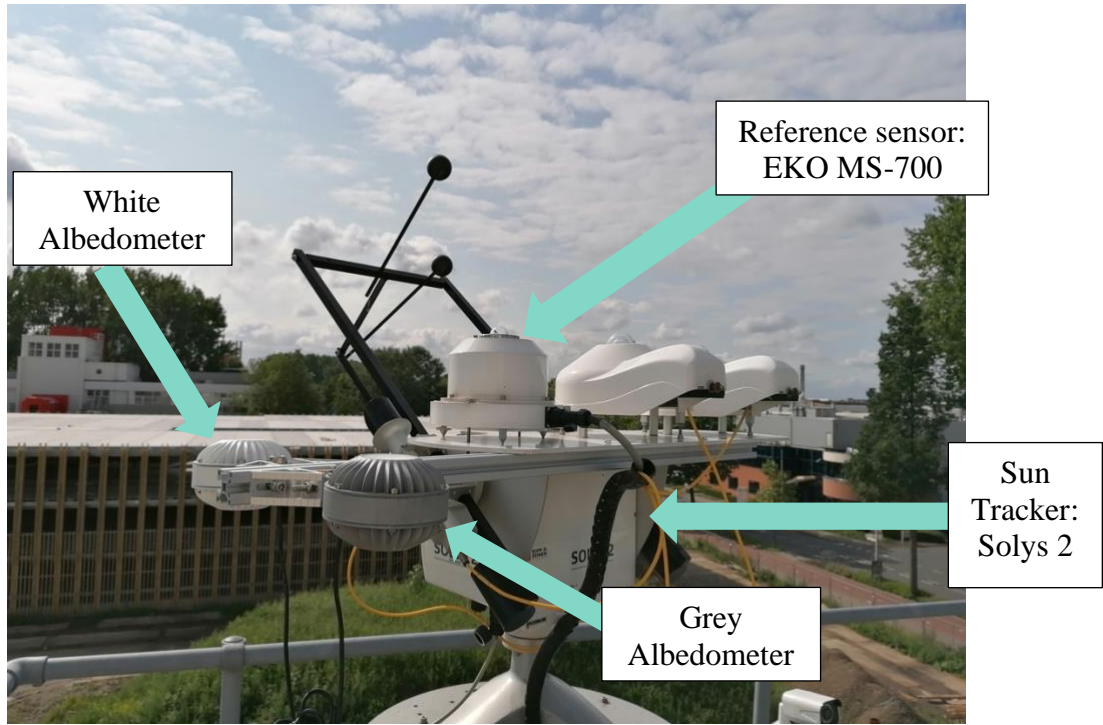
Figure 48: Sensors placed at the monitoring station next to reference sensor.

The sensors (white and grey versions) were installed on the roof as close to the reference sensor (EKO Spectroradiometer MS-700) as possible (Figure 48). Both sensors were connected to a Raspberry Pi computer with a USB-Ethernet-USB connection cable of approximately 25m. Measurements were carried on during 23-27 August 2021, but only a few hours were successfully recorded each day. The data retrieved from the sensors were compared to the reference data simultaneously to obtain a calibration factor. This calibration factor will be validated with measurements from a different time to analyse the accuracy of the calibration. Some limitations during calibrations were:

- It is unknown when was the last time the reference sensor was calibrated. Not knowing when the sensor was last calibrated makes the calibration less accurate as one is not sure how accurate are the measurements yielded by that sensor.
- The calibration factor of the EKO spectroradiometer is unknown. The calibration factor of the reference is needed to have a more accurate calibration of the device.
- Data from the EKO spectroradiometer gives the spectral irradiance to per nano-meter resolution and every minute. In contrast, the albedometer gives data every second for three different wavelength ranges: 320-590nm, 590-850nm and 850-

1100nm. Data is integrated from both sensors to match the resolution. Integrating data reduces the possibility to get a more accurate calibration factor.

- If there were value errors, the computer would stop running, and data was lost. This error was fixed but restricted the amount of data that was collected.

- For some days, the albedometers collected data. However, those cannot be compared to reference values because there are some days when the reference does not have any available recorded.

- The monitoring station went into maintenance, and the power was shut down for four days, limiting, even more, the amount of data that was collected.

- There appears to be a short circuit in the non-filtered photodiode of the white sensor (up-facing). Sometimes the photodiode works well, but at some moments, the current reduces considerably. This behaviour is intermittent and makes it complicated to use an extensive data set for calibration.

- The temperature in the down-facing grey sensor has unexpected behaviour and rises more than 20 degrees in seconds, compromising the measurements. This problem can be due to electrical problems.

- There was no reference sensor for the down-facing measurements. Consequently, the albedo estimations cannot be calibrated properly. The correction factors for the up-facing sensors will be used to calibrate the down-sensors.

6.1. Calculation of Irradiance

Before determining the calibration factor, the current measured by the albedometers had to be converted into irradiance. To obtain irradiance (W/m^2) from current (A), it must be divided by the sensitivity of the photodiode (A/W) and its active area (m^2) (6) [8]. The sensitivity of the photodiodes was taken as the average of the sensitivity values over the three desired spectrums (0.52 A/W). This information was taken from the datasheet of the photodiode. The active area of the photodiode is 13 mm^2.

$$E = \frac{I}{S \cdot A} \qquad (6)$$

To include the temperature dependency of photodiodes' response, temperature coefficients were estimated by analysing the correlation between the increment in temperature and the rise or decrease in current measured at a constant irradiance. The temperature coefficients (T_c) were estimated for all three photodiodes in white and grey sensors by estimating the correlation between variation in current and temperature increments (Table 11). Additionally, the transmittance (%T) losses from the diffuser and optical filters and the view factor (see Section 3.1) were also considered correction factors for the measurements (See Appendix). Since the transmittance of both diffusers and filters are not constant during the wavelength ranges, the average transmittance within the spectral ranges was used. The view factor correction accounts for the 0.7% loss of light intensity from the diffuser to the photodiodes. The reference temperature is 25ºC. Equation (6) was adapted as follows to calculate the irradiance taking into consideration these three components:

$$E = \frac{I + (\Delta T \cdot T_c)}{S \cdot A \cdot \%T \cdot VF} \qquad (7)$$

Where I is the measured current in µA, ΔT is the difference between the operating temperature and the reference temperature, T_c is the temperature coefficient, A is the active area of the photodiode, S is the average sensitivity of the photodiode, $\%T$ is the percentage of transmittance accounting for both diffuser and filter's transmittance characteristics, and VF is the View factor.

Table 11: Temperature Coefficients for every photodiode in each albedometer estimated for the up-facing sensor. The down-facing sensor will be assumed to have the same temperature dependency.

Photodiode (Range measured)	Grey Sensor Temperature Coefficient [µA/ºC]	White Sensor Temperature Coefficient [µA/ºC]
HM (590-1100 nm)	-0.615	-0.108
LP (850-1100 nm)	0.288	0.054
NF (320-1100 nm)	0.2411	-0.013

This yields values in the ranges showed in Table 11, to obtain the desired wavelengths (320-590nm, 590-850nm & 850-1100nm) the following equations were implemented:

$$E_{320-590\,nm} = E_{320-1100\,nm} - E_{590-1100\,nm} \qquad (8)$$

$$E_{590-850\,nm} = E_{590-1100\,nm} - E_{850-1100\,nm} \qquad (9)$$

$$E_{850-1100\,nm} = E_{850-1100\,nm} \qquad (10)$$

6.2. Calibration Factor

The output of the white and grey albedometers and the EKO spectroradiometer were compared to determine the calibration factor. The reference data is recorded every minute interval and is compared to the exact timestamp of the testing sensor output. In Figure 49, one can see the comparison between the irradiance measured by the spectroradiometer and the grey sensor. The error of this sensor was calculated using Equation (11) for each range and averaged to be 36.31% (Table 12). Figure 50 shows the performance of the white sensors at the three wavelength ranges and for the full spectrum. For the white sensor, the average error was found to be 24.01% (Table 13).

It is essential to mention that two sets of data of different days were used to calibrate the device since only two hours could be used for calibration from the six days where data was collected. Not enough data was available due to a malfunction in one of the photodiodes of the up-facing white sensor and additional problems related to the data collection software. It is important to recall that sky conditions during both sets of calibration were not the same. During the 40 minutes measured on the 23rd of August, sky was clear, while there were some clouds during the hour and 20 minutes used from the 26th of August. This will reduce the accuracy of the correction factor obtained. The figures shown in this section represent only one set of data.

$$\% \, Error = \frac{E_{sensor} - E_{EKO}}{E_{EKO}} \qquad (11)$$
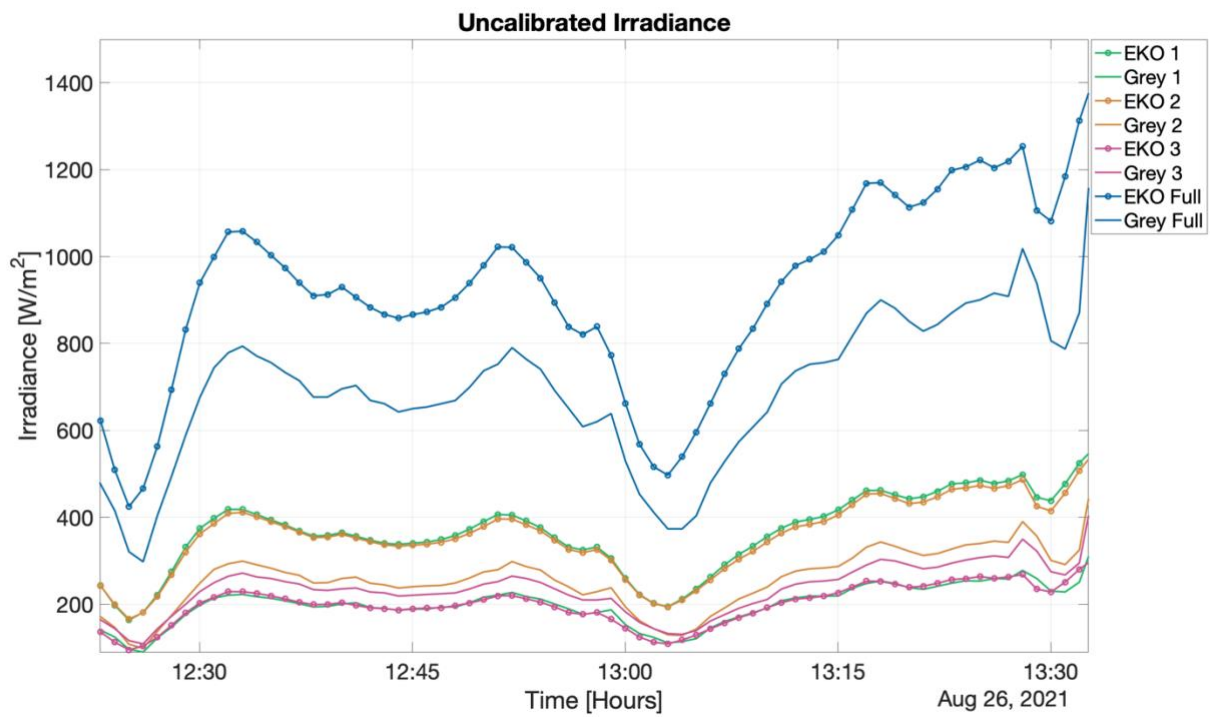
Figure 49: Uncalibrated spectral Irradiance of grey sensor and spectral irradiance measured by the reference sensor. Data is plotted for the three spectrums ranges. 1 corresponds to 320-590nm, 2 corresponds to 590-850nm and 3 corresponds to 850-1100nm. 'Full 'gives the Irradiance values for the full spectrum.
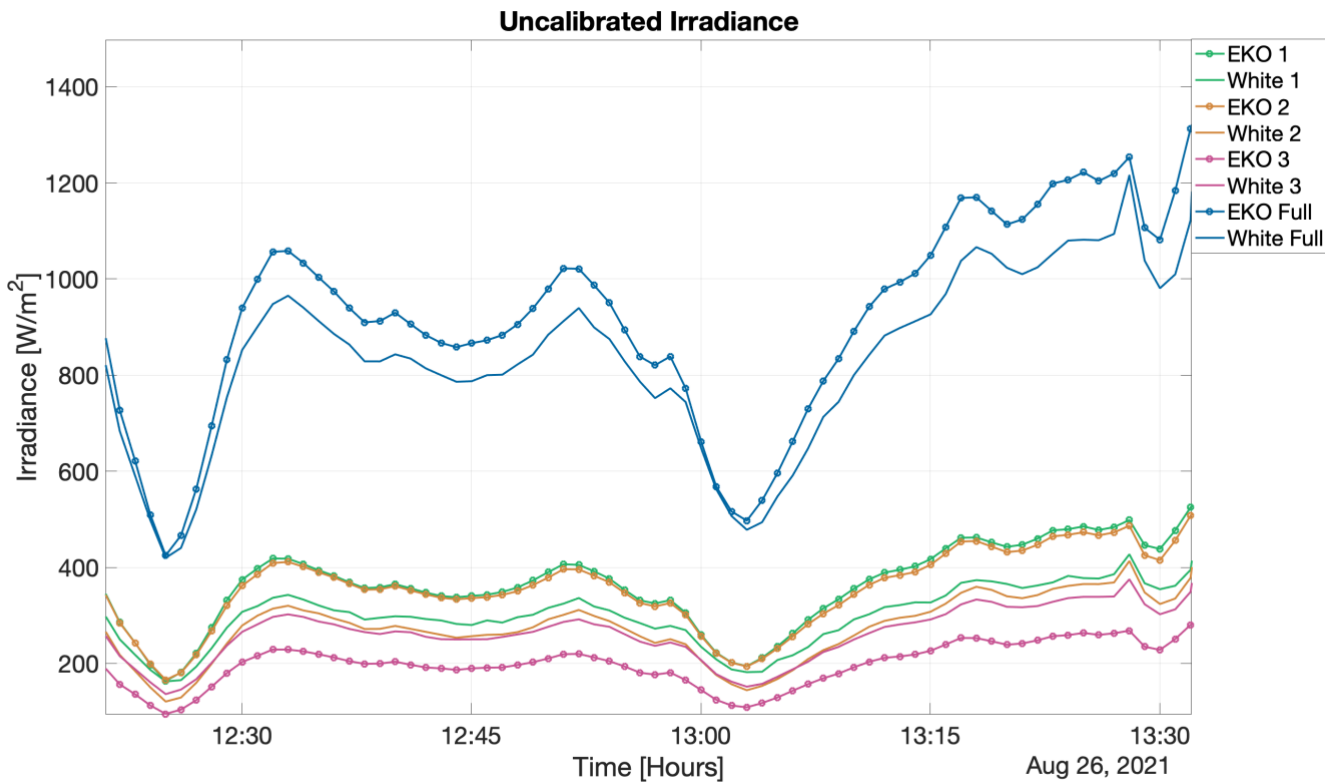
Figure 50: Uncalibrated spectral Irradiance of white sensor and spectral irradiance measured by the reference sensor. Data is plotted for the three spectrums ranges. 1 corresponds to 320-590nm, 2 corresponds to 590-850nm and 3 corresponds to 850-1100nm. 'Full 'gives the Irradiance values for the full spectrum.

Table 12: Error for uncalibrated grey sensor from two sets of measurements. Shows the deviation of the measurements to the reference value.

Wavelength Range	Error Grey Sensor (up-facing) 23-Aug-2021	Error Grey Sensor (up-facing) 26-Aug-2021	Error Grey Sensor (up-facing) Average
320 – 590 nm (1)	54.55%	45.48%	50.01%
590 – 850 nm (2)	35.92%	27.98%	31.95%
850 – 1100 nm (3)	34.08%	18.26%	26.17%
Weighted Average Error over the full spectrum (320–1100nm)	41.72%	30.89%	**36.31%**

Table 13: Error for uncalibrated white sensor from two sets of measurements. Shows the deviation of the measurements to the reference value.

Wavelength Range	Error White Sensor (up-facing) 23-Aug-2021	Error White Sensor (up-facing) 26-Aug-2021	Error White Sensor (up-facing) Average
320 – 590 nm (1)	14.77%	17.15%	15.96%
590 – 850 nm (2)	17.06%	22.23%	19.64%
850 – 1100 nm (3)	41.40%	33.30%	37.35%
Weighted Average Error over the full spectrum (320–1100nm)	23.95%	23.99%	**24.01%**

The ratio between the irradiance measured by the reference to the sensor output is average for each spectrum to determine the calibration factor. This calibrated factor is later multiplied by the uncalibrated irradiance to obtain a calibrated value. It is important to remember that since this calibration did not follow any standard procedure, the correction factor will not be accurate for all measurements and could vary when different sky conditions are present (More sunny or more cloudy days). Figure 51 and Figure 52 show the calibrated spectral irradiance of both grey and white sensors compared to the reference.
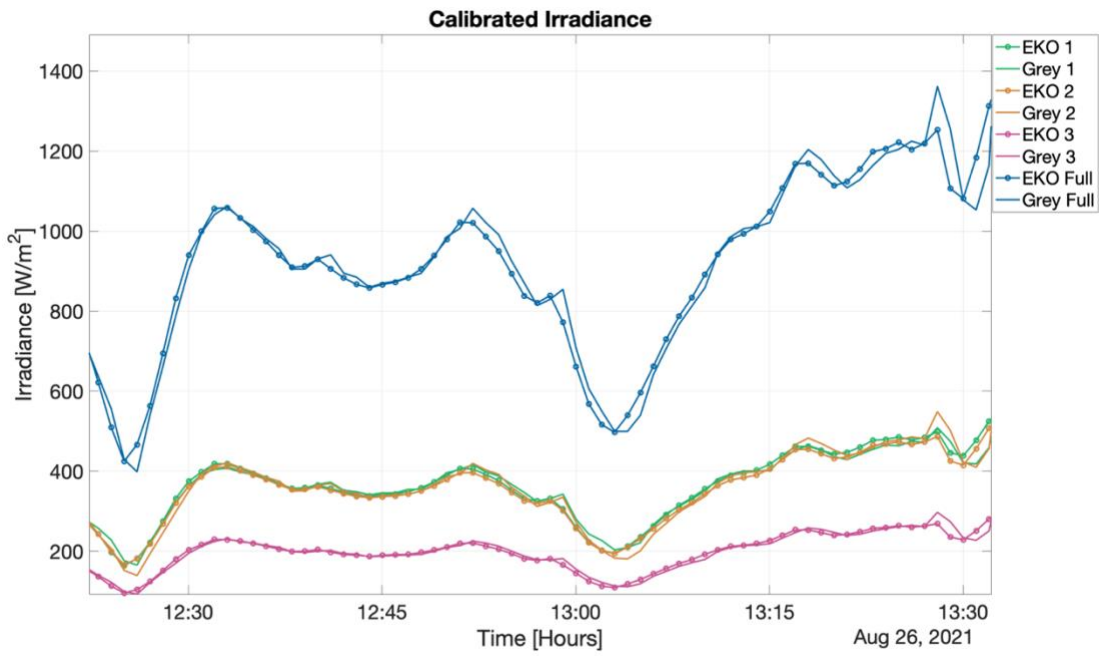
Figure 51: Calibrated spectral Irradiance of grey sensor and spectral irradiance measured by the reference sensor. Data is plotted for the three spectrums ranges. 1 corresponds to 320-590nm, 2 corresponds to 590-850nm and 3 corresponds to 850-1100nm.
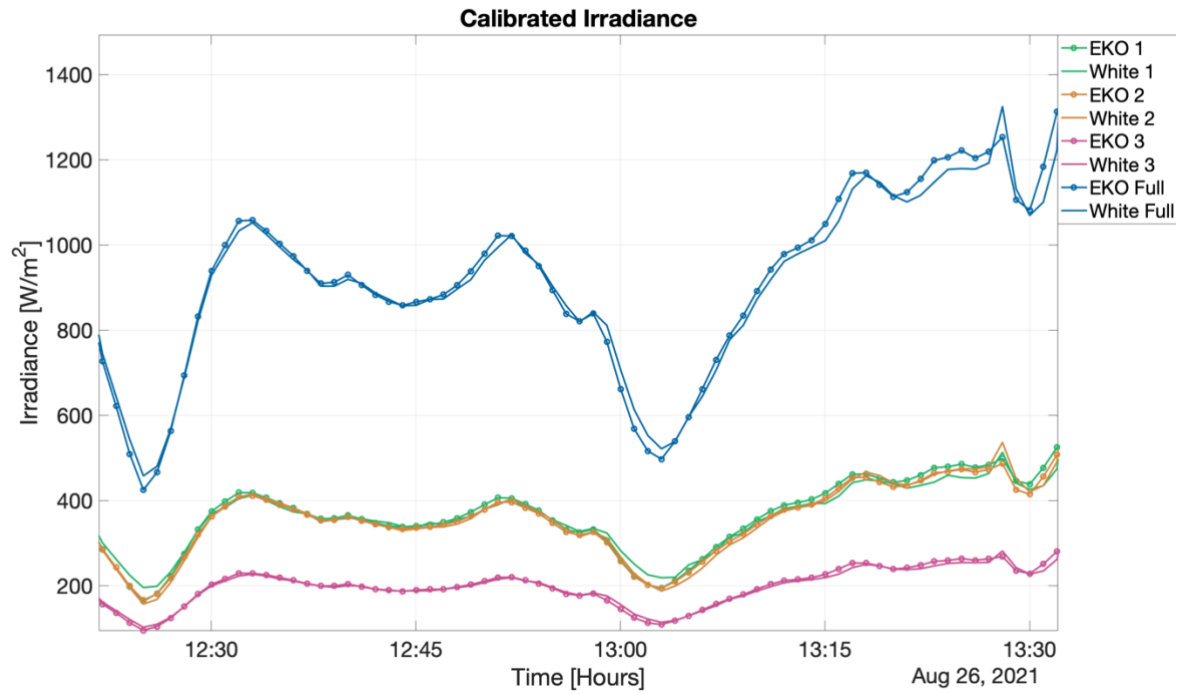

Figure 52: Calibrated spectral Irradiance of white sensor and spectral irradiance measured by the reference sensor. Data is plotted for the three spectrums ranges. 1 corresponds to 320-590nm, 2 corresponds to 590-850nm and 3 corresponds to 850-1100nm.

In the spectrally calibrated irradiance, one can see that the reduction of the difference between the reference data and the estimated data is shallow. The average error of each sensor was reduced to 3.04% for the grey sensor and 1.10% for the white sensor (See Table 14 and Table 15). Additionally, the temperature for the white and grey sensors was plotted in Figure 53 . One can see that the grey sensors keep having an average of 8ºC higher operation temperature than the white sensors, as estimated in Section 5.2. This difference could be either due to the colour, which absorbs more light or due to the higher transmittance of the N-BKT diffuser.

Table 14: Error for calibrated white sensor from two sets of measurements. Shows the deviation of the measurements to the reference value.

Wavelength Range	Error White Sensor (up-facing) 23-Aug-2021	Error White Sensor (up-facing) 26-Aug-2021	Error White Sensor (up-facing) Average
320 – 590 nm (1)	1.98%	0.45%	1.21%
590 – 850 nm (2)	2.32%	0.96%	1.64%
850 – 1100 nm (3)	0.84%	0.02%	0.43%
Weighted Average Error over the full spectrum (320–1100nm)	1.72%	0.48%	**1.10%**

Table 15: Error for calibrated grey sensor from two sets of measurements. Shows the deviation of the measurements to the reference value.

Wavelength Range	Error Grey Sensor (up-facing) 23-Aug-2021	Error Grey Sensor (up-facing) 26-Aug-2021	Error Grey Sensor (up-facing) Average
320 – 590 nm (1)	4.02%	0.27%	2.14%
590 – 850 nm (2)	2.72%	1.27%	1.99%
850 – 1100 nm (3)	9.82%	0.43%	5.12%
Weighted Average Error over the full spectrum (320–1100nm)	5.44%	0.65%	**3.04%**
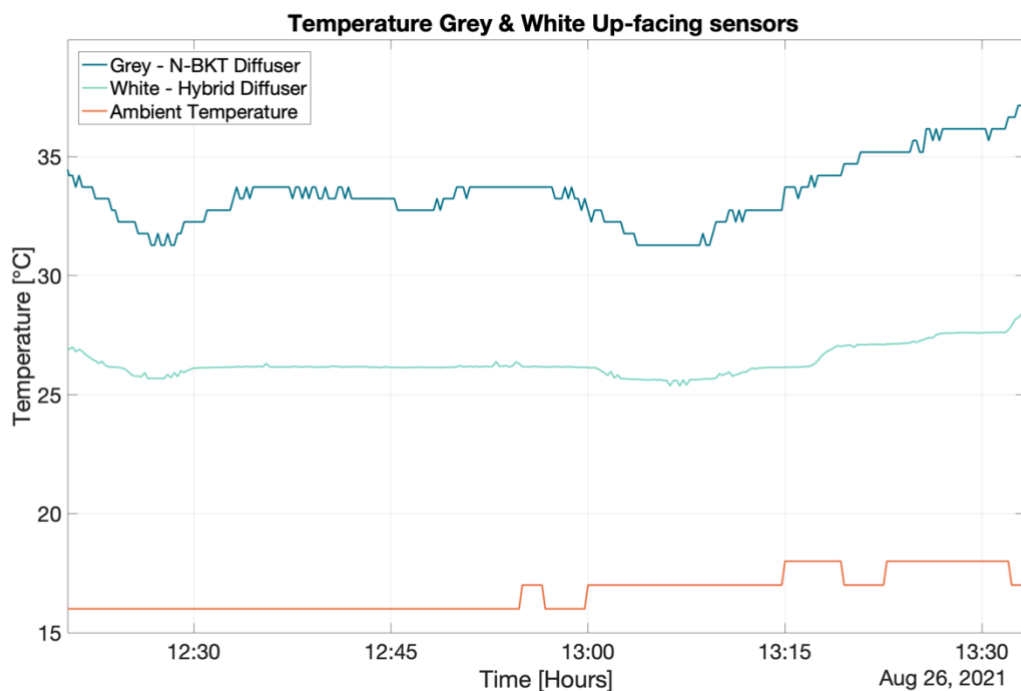
Figure 53: Operating temperature of grey and white sensors during calibration.

The final calibration factors (Table 16) were estimated by averaging the calibration factors found for each data set. This calibration factors will be used for

validating this approach and estimating the accuracy and precision of the instruments. It was not possible to estimate calibration factors for the down-facing sensors because there was no reference instrument available for reflected irradiance.

Table 16: Calibration factors per wavelength range and per sensor

Wavelength Range	Calibration factors grey sensor (up-facing)	Calibration factors white sensor (up-facing)
320 – 590 nm (1)	1.993	1.191
590 – 850 nm (2)	1.546	1.266
850 – 1100 nm (3)	0.834	0.725
320 – 1100 nm (Full)	1.402	1.071

7. Validation

Validation of the calibration factors obtained in Section 6.2 had to be done to estimate their accuracy. The same procedure as from calibration was used to analyse and compare the output data of all sensors. Data from a different day was multiplied by the previously calculated calibration factors. In Figure 54 and Figure 55, the calibrated irradiance for validation of the correction factors is compared to the reference spectroradiometer. The sensors' error before calibration can be found in Table 17, with an average error of 42.62% for the grey sensors and 28.33% for the white sensor.

Table 17: Error uncalibrated spectral irradiance 27 Aug 2021

| Wavelength Range	Error Grey Sensor (up-facing)	Error White Sensor (up-facing)
320 – 590 nm (1)	66.2%	30.27%
590 – 850 nm (2)	48.49%	17.96%
850 – 1100 nm (3)	11.15%	37.11%
Weighted Average Error over the full spectrum (320–1100nm)	42.62%	28.33%
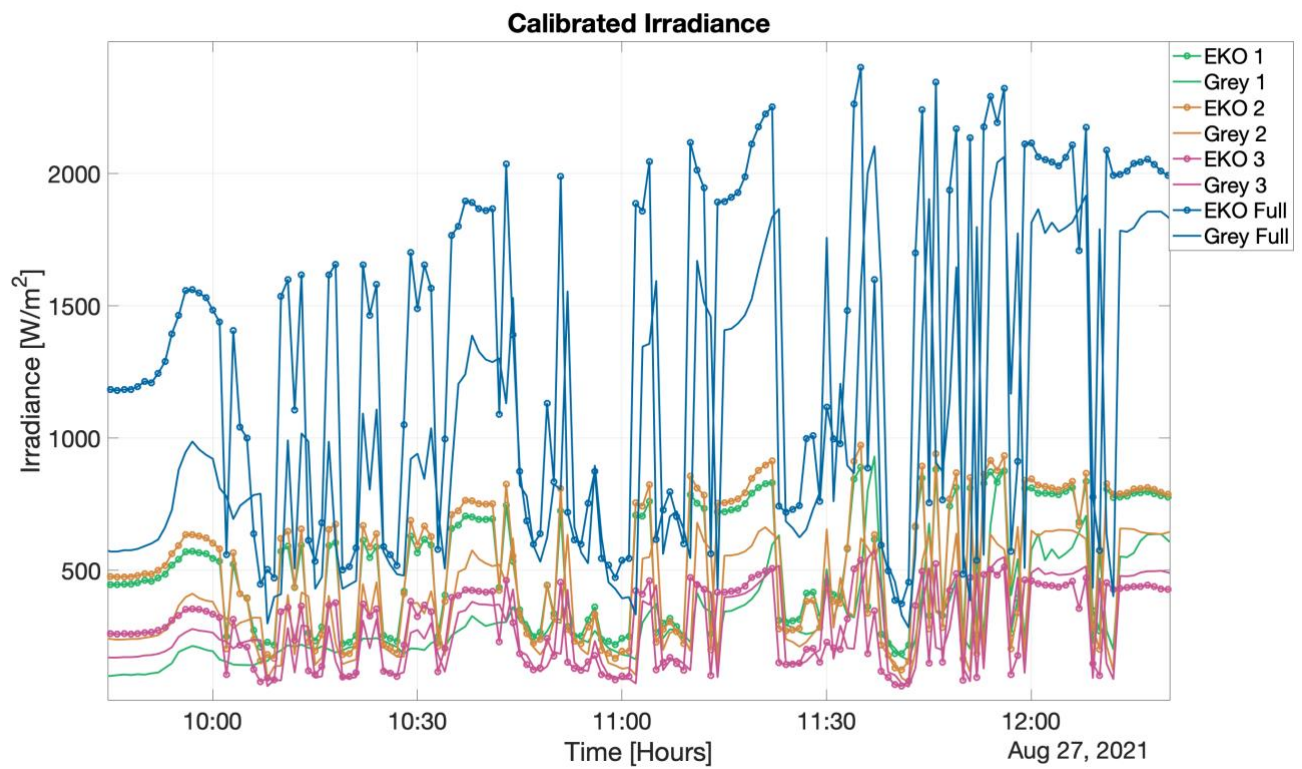
Figure 54: Calibrated Irradiance for validation of grey sensor' correction factor
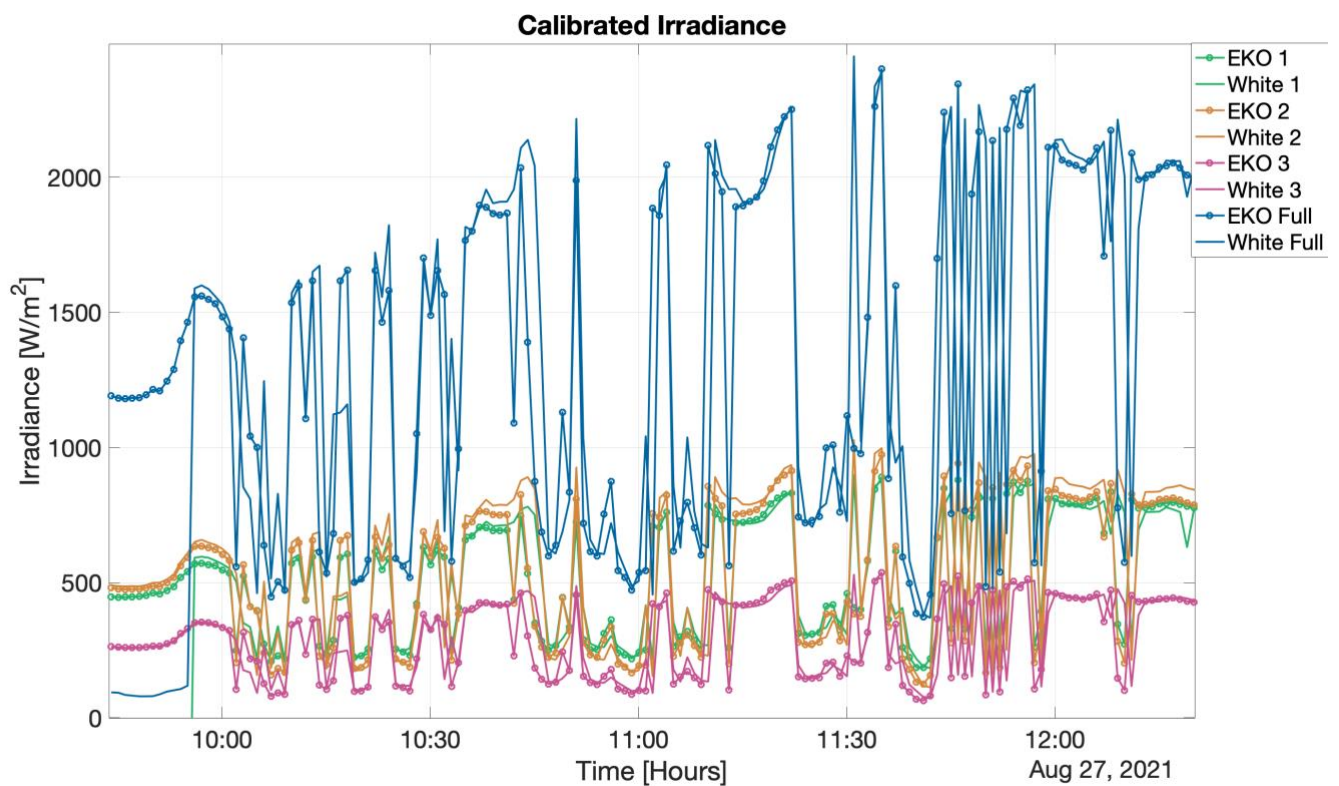

Figure 55: Calibrated Irradiance for validation of white sensor' correction factor

Error in both sensors was reduced considerably after calibration, the grey sensor's average error reduced to 20.4% and the white sensor's error dropped to 7.3%. However, the final errors after validation are more significant than in the error after calibration for both sensors. The increment in the error percentage was expected due to the small data that was available. For a better estimation of the calibration coefficient, one should consider data from several days and the calibration factor of the reference sensor.

Table 18: Comparison of error after calibration to error after validation for grey sensor

Wavelength Range	Error Grey Sensor after calibration (up-facing)	Error Grey Sensor after validation (up-facing)	Error difference between calibration and validation
320 – 590 nm (1)	2.14%	32.63%	30.49%
590 – 850 nm (2)	1.99%	20.36%	18.64%
850 – 1100 nm (3)	5.12%	7.28%	2.16%
Weighted Average Error over the full spectrum (320–1100nm)	3.04%	**20.40%**	17.44%

Table 19: Comparison of error after calibration to error after validation for white sensor

Wavelength Range	Error White Sensor after calibration (up-facing)	Error White Sensor after validation (up-facing)	Error difference between calibration and validation
320 – 590 nm (1)	1.21%	16.92%	15.71%
590 – 850 nm (2)	1.64%	3.86%	2.22%
850 – 1100 nm (3)	0.43%	0.48%	0.05%
Weighted Average Error over the full spectrum (320–1100nm)	1.10%	**7.30%**	6.19%

Since the only two differences between the grey and white albedometers are their colours and the diffuser, one can assume that this plays a significant role in the higher error percentages presented by the grey sensor. There are two possible causes for this. First, the hybrid diffuser in the white sensor has better scattering properties and cosine response; it is expected to distribute light more uniformly inside the device, increasing the precision of the measurements. Second, the lower temperature in the white sensor due to the lower transmittance of the diffuser (and lower surface temperature of the casing) reduces the noise and effects in the responsivity of the photodiodes. The lower error difference between calibration and validation values for the white-hybrid diffuser configuration can indicate the better precision of this instrument than the grey-N-BKT albedometer.

7.1. Calculation of Albedo

As mentioned in Section 1.2, albedo is given as the ratio between the power of the reflected light and the total incoming light. The surface below the albedometers is mainly composed of pea gravel. The exact type of gravel is unknown. however, it will be assumed to have an average albedo of 0.24 which is typical for medium blends (not dark nor white colours) [20]. For this calibration, the reflected irradiance was not measured by the reference sensor. Consequently, the data cannot be compared to reference values, and it is impossible to obtain calibration factors for the down-facing sensor, as in the previous section. The calibration factors obtained in the previous section for the up-facing sensor will be used to calculate the irradiance of the down-facing sensors. Later, this reflected irradiance will be used to calculate the albedo with the following equation.

$$Albedo = \frac{E_{down-facing\ sensor}}{E_{up-facing\ sensor}} \qquad (12)$$
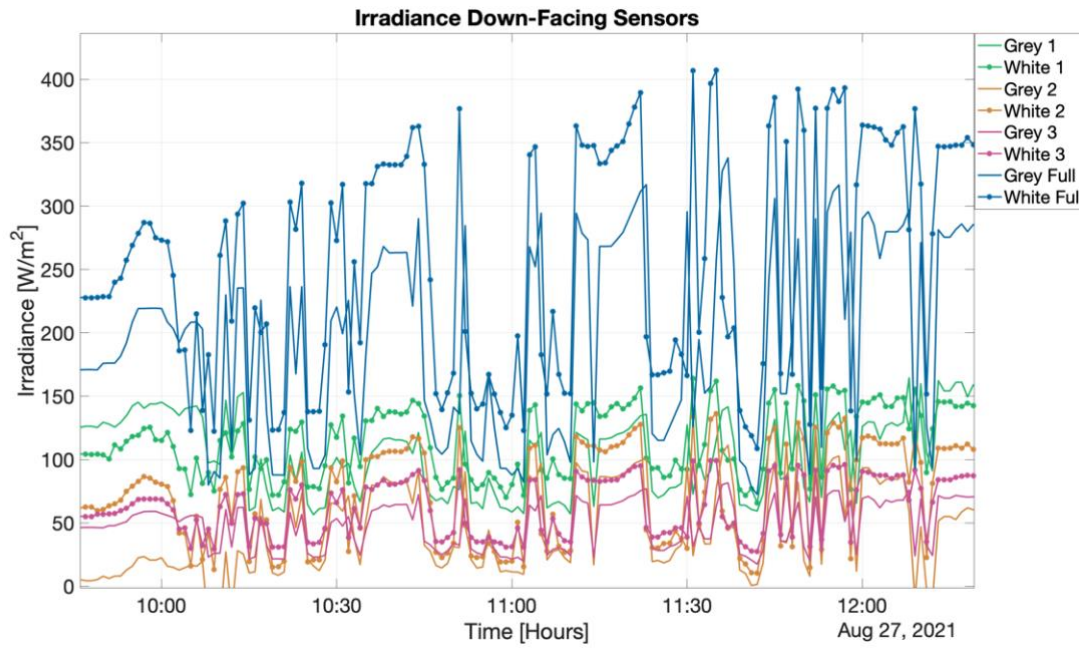
Figure 56: Calibrated Down-facing Irradiance for grey and white sensors
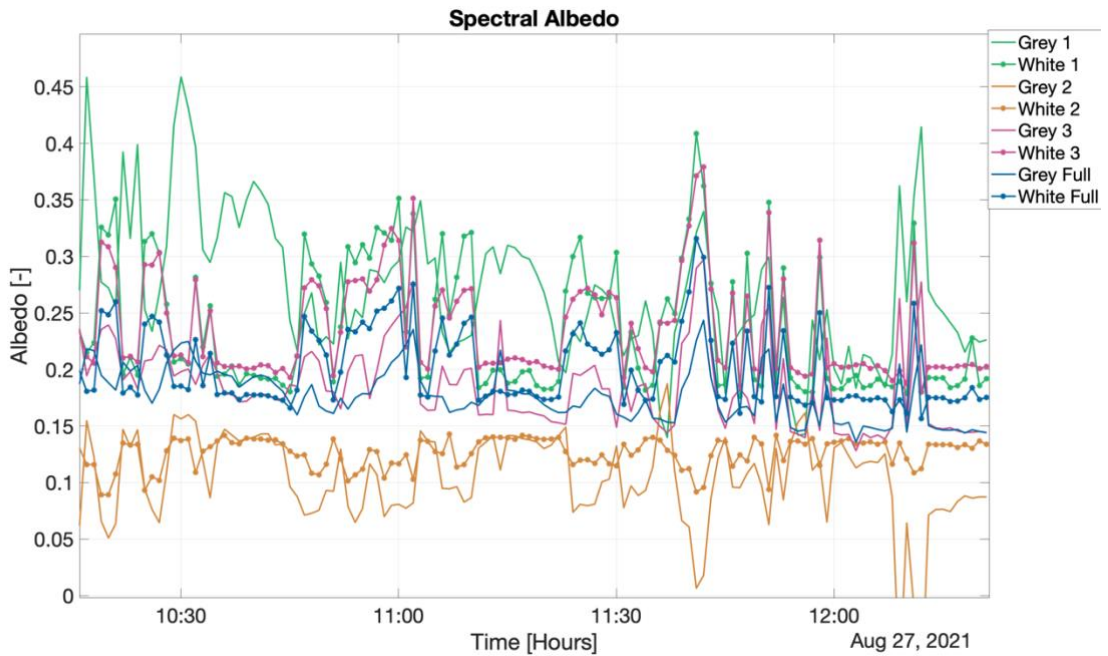
Figure 57: Spectral albedo of grey and white sensors

In Figure 58, the temperature of the grey sensor shows an unexpected behaviour since it rises over 20 ℃ in a few seconds. Electrical problems either with one photodiode or the temperature sensor can be the cause of this malfunction. This can cause an increment of the error of albedo estimations. In Figure 57 one can see than when this

temperature step happens, there is a bigger offset in the grey sensor's measurements for wavelength ranges 1 and 2 (320-590nm and 590-850nm). Estimated albedo values are shown in Table 20.
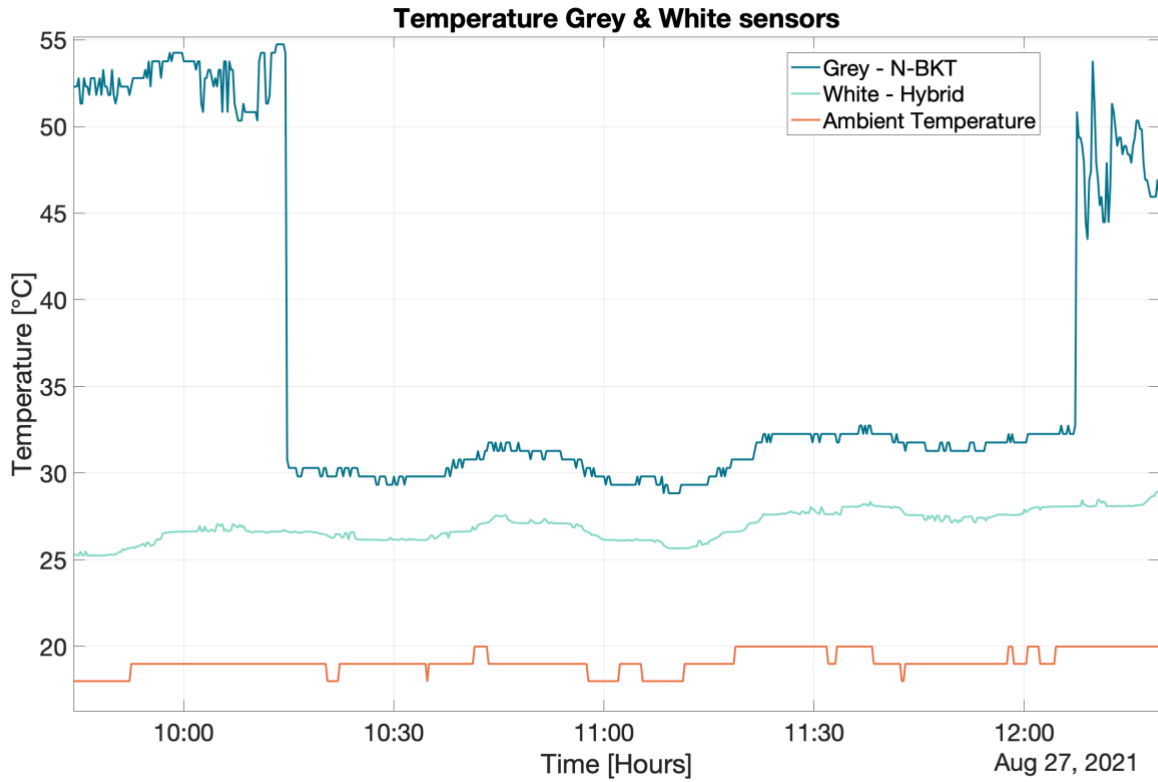
Figure 58: Temperature of down-facing grey and white sensors

The calculated albedo values (Table 20) differ for both sensors. The lower albedos measured by the grey sensor could be explained by temperature variation in its down facing. Especially for the 590-850 nm range, which was shown previously directly affected by it. If these values are compared to the average gravel albedo (0.24), both sensors had close approximations. For the grey sensor, the difference of the average albedo is of only 0.02 and for the white sensor is of 0.05. However, these calculations are only a reference since there was no data available for the actual albedo of the surface.

Table 20: Spectral average albedo of grey and white albedometers

Wavelength Range	Average Albedo Grey Sensor	Average Albedo White Sensor
320 – 590 nm (1)	0.3783	0.2096
590 – 850 nm (2)	0.0845	0.1265
850 – 1100 nm (3)	0.1996	0.2348
Weighted Average over the full spectrum (320–1100nm)	0.2229	0.1897

7.2. Additional specifications

Minimum irradiance

The minimum irradiance the instruments measure was estimated by comparing the time in the morning that the sensors start measuring with the operating times of the EKO spectroradiometer. Sun position was estimated using an online solar calculator and should be consider only as an approximation [21]. Figure 59 and Figure 60 show this comparison. The EKO spectroradiometer recorded data since 6:00 h (<1 W/m^2 and ~1.53º altitude) in the morning. However, the white sensor started to register data from 6:48 h (~8.55º altitude), the recorded irradiance by the reference at that time was of 13.76 W/m^2. The grey sensor measured data from 6:26 h (~5.25º altitude) at a solar irradiance of 12.76 W/m^2. During the selection of the diffuser, it was expected for the white sensor to have a considerably higher minimum irradiance due to the very low transmittance of the hybrid diffuser. However, this was not the case. There are two possible reasons behind this outcome. First, the transmittance is considered for the estimation of the irradiance (7), so even if the current measured is very low, it can be converted into irradiance values. Second, the hybrid diffuser has better cosine response than the N-BKT diffuser, allowing the diffuser to scatter light evenly for lower angles of incidence.
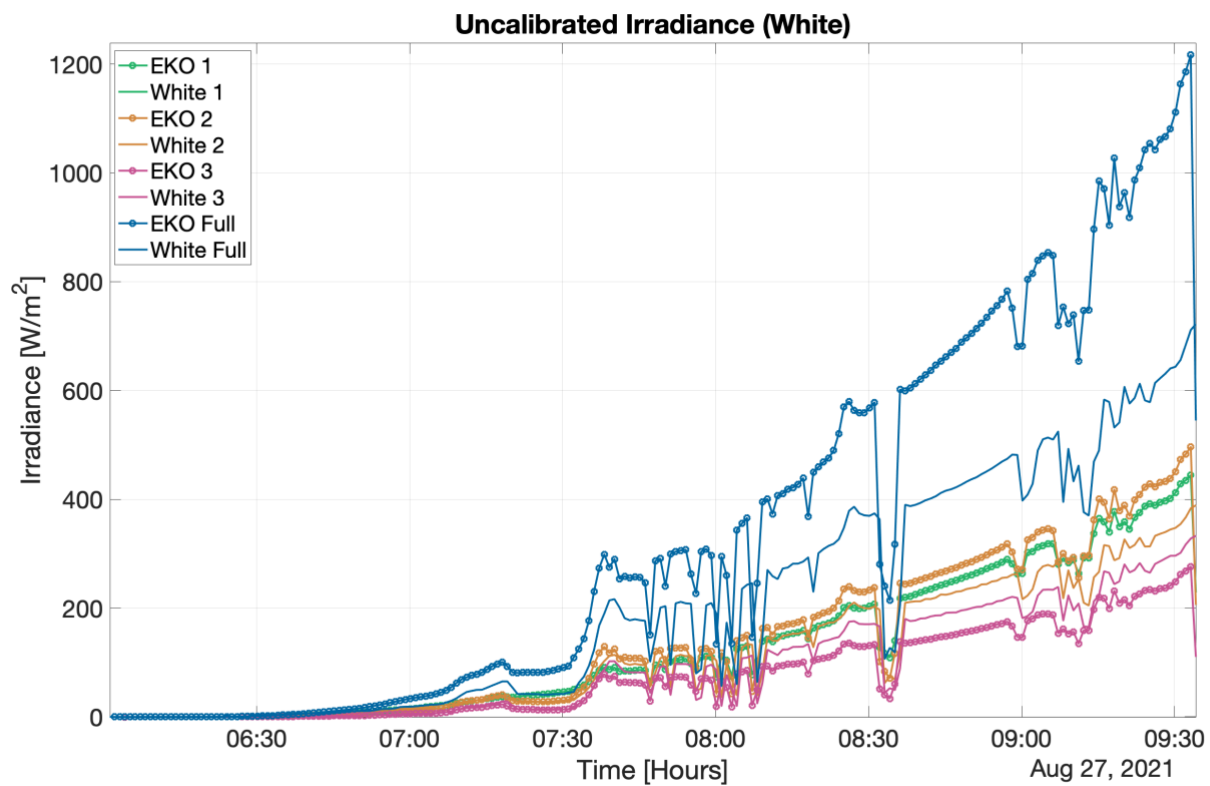
Figure 59: Uncalibrated Irradiance of white sensor showing the time in the morning it starts measuring
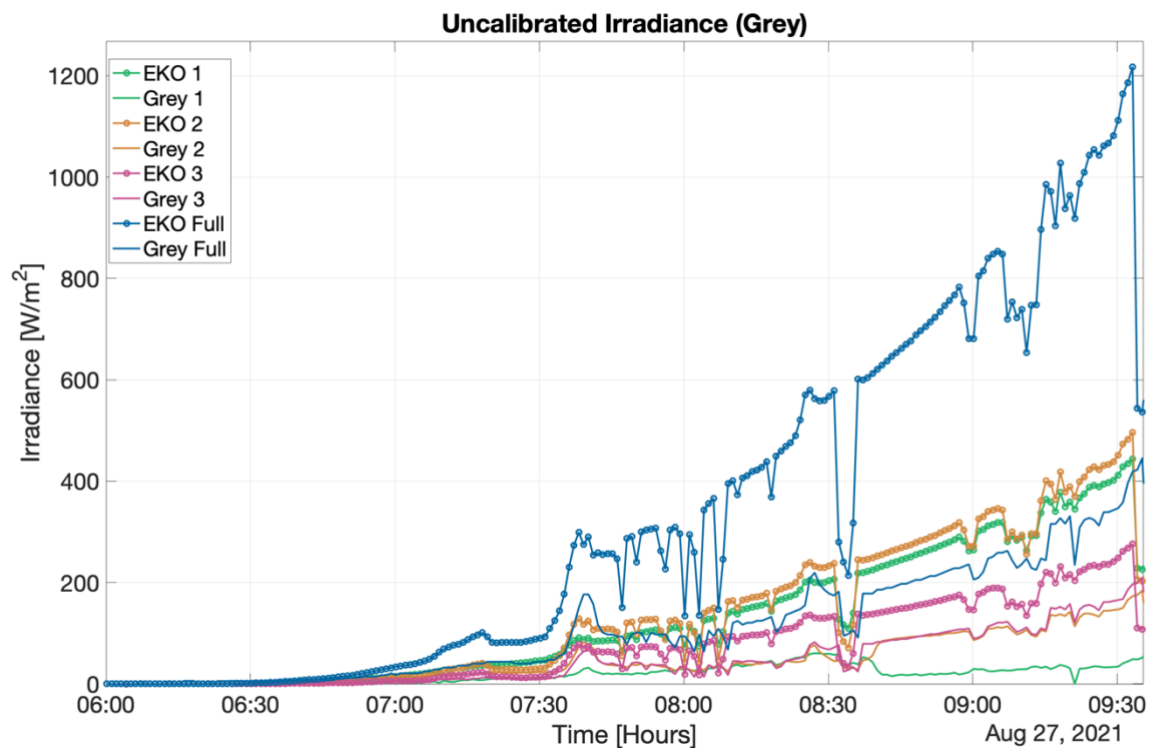
Figure 60: Uncalibrated Irradiance of sensor showing the time in the morning it starts measuring

Operating temperature of photodiodes

In previous sections, the difference in temperature for both versions of the final prototype have been compared and shown to be 8ºC higher for the grey-N-BTK diffuser configuration. However, the average working temperature of the photodiodes was not compared to the ambient temperature. This was estimated by comparing the internal temperature of the device to the ambient temperature during operation. The average temperatures for the two calibration data sets and the validation data set were considered for this estimation. The results are shown in the table below. The higher operating temperature of the down-facing sensor is due to issues with the electrical components in the PCB.

Table 21: Photodiodes operational temperature above ambient temperature

Albedometer configuration	Average operating temperature above ambient temperature (Up-facing sensor) [ºC]	Average operating temperature above ambient temperature (Down-facing sensor) [ºC]
Grey – N-BTK Diffuser	17	20.75
White – Hybrid Diffuser	8.66	6.89

8. Discussion and recommendations

The work presented here aimed to increase the accuracy of the spectrally-resolved pyranometer previously designed by Annanta Kaul [8] by improving its optical, electrical, and mechanical properties. Additionally, electrical and mechanical characteristics were changed to have two pyranometers integrated, one up-facing and one down-facing, to measure the spectral albedo.

Optical Design

The optimal distance between the photodiodes and the diffuser was found to estimate a view factor. It was found that the optimal distance between the diffuser and the photodiodes is 2.9mm. With this distance, a view factor of 99.3% was obtained. It was impossible to achieve 100% due to the geometry of the casing and the filters' thickness, which means that 99.3% of light transmitted by the diffuser will reach the photodiodes. The 0.7% missing was added to the correction factors for the equation used to estimate

the irradiance. This approach was evaluated through experiments. It was found that reducing the distance between the diffuser eliminated the shadowing and increased the detected current by all photodiodes. The angle maximum angle of incidence was improved from 30º to 80º.

Regarding the separation of the spectrum in three different wavelength ranges, new filters were selected. The new filters have higher transmittance, create sharp wavelength ranges, and reduce the cost of the filters by around 86%. The selected filters are sold in 20 different cut-on wavelengths, which could be beneficial if one wants to have additional photodiodes and measure the spectrum in smaller wavelengths ranges. Currently, the device measure three parts of the spectrum (320-590nm, 590-850, 850-1100). However, it was a desire to measure from 300 to 1200nm because it is approximately the range in which c-Si PV cells (which currently account for a big part of the PV market) operate. However, it was limited to 320 to 11000nm due to the photodiode's specifications.

The diffuser selection was made to improve the poor scattering properties that the old diffuser presented at higher wavelengths. Since it was impossible to measure scattering properties, the decision was made entirely on the manufacturer's specifications. Both the old (N-BKT Ground Glass) and selected (Hybrid) diffusers made it to the final prototype to compare if it was worth reducing the transmittance to have better scattering properties and angular response. During outdoor operations, it was concluded that the lower transmittance has a positive effect on the reduction of the operating temperature of the device. The white sensor operates at around 8ºC lower than the sensor with the N-BKT diffuser. Additionally, the lower transmittance has little effect on the minimum measured irradiance since the difference is only of 1 W/m^2.

Electrical Design

The PCB assembly integrates both up-facing (global irradiance) and down-facing (reflected irradiance) sensors. The reduction in the size of the PCB gave more freedom to the casing design and helped implement the changes in the optical configuration.

However, having all electrical components closer together can increase the operating temperature. The black-coated PCB, which help reduce light pollution inside the device, also affects the temperature due to higher light absorption. Additionally, there is a problem with one of the photodiodes in the up-facing sensor of the White-Hybrid prototype. The photodiode sometimes measures correctly, and sometimes it does not measure or measure minimal current. This can be due to a short circuit. Another short-circuit is probably present in one of the components of the down-facing sensor of the Grey-N-BTK configuration, probably the temperature sensor itself. During calibration and validation, the temperature in this sensor rises suddenly over 20º and increases more than in the up-facing sensor. These problems compromised the amount of data available for calibration and the reliability of some of the measurements.

Mechanical Design

The bio-inspired design of the casing was proven to be beneficial for reducing the operating temperature of the device. The surface temperature of the ribbed version versus the non-ribbed version is around 2ºC lower. This matches the 1 to 2ºC rise of surface temperature found in Cacti without ribs [18]. The operating temperature varies around 2.7ºC within the ribbed and non-ribbed versions of the casing (having the same diffuser) in laboratory conditions. In the final prototypes, under outdoor conditions, the operating temperature for the white sensor is 8.6ºC above ambient temperature and 17ºC for the grey sensor. As a reference, the photodiodes inside LI-COR LI-200 pyranometers operate at 6ºC above ambient temperature [22]. Since the geometry, material, and electrical components are the same for both configurations, it is possible to assume that the diffuser's transmittance and the device's colour play a role in this difference. However, to assess what the weight of each characteristic in this is, one should perform additional temperature tests blocking the diffuser.

Calibration and Validation

Calibration of the device had a lot of limitations see Section 6.2. the main limitation was the reduced data. From six days that the sensors were supposed to measure data, only 2

hours were useful for calibration. Having such little amount of data to compare the prototypes did not yield accurate correction factors. However, they did reduce the deviation between the measured irradiance and the expected irradiance even after validation. First, the calibration was made only with one data set, but it was improved by adding another set of measurements, even though they were only a few hours of performance. This confirms the necessity of more extensive sets of data. After validation, the sensors have an average accuracy of 7.3% and 20.4% for the white and grey sensors, respectively.

Nevertheless, the percentage of error within both devices before calibration is very similar between data sets, indicating that the sensors' precision is good. Finally, the sensors' minimum irradiance to operate is 13.76 W/m^2 and 12.76 W/m^2 for the white and grey sensors respectively. This difference was expected to be more prominent due to the lower transmittance in the white sensor's diffuser. However, it may have been corrected by the correction factors implemented when estimated the irradiance, or it is compensated by the better cosine response of the device's diffuser.

Recommendations

- It was not possible to measure the cosine response of diffuser due to problems with in-lab measurement setup equipment. Having the cosine response could be beneficial to have a better estimation of the effect of the Sun's position on the data measured by the device

- For the selection of the diffuser, only flat diffusers were considered. Domes or quartz diffusers can be a good option to explore, but they may increase the cost of the sensor considerably.

- A photodiode in the up-facing of the white albedometer probably has short-circuit issue, and the down-facing temperature sensor of the grey albedometer presents an odd behaviour. It is advised to check all the elements in the PCB assembly to correct this.

- The casing can be improved by eliminating or changing the cable used to connect the PCB to a computer. This would allow the design to have ribs all over the surface. This cable also limits the size of the casing.

- The time when the desiccant must be changed was not estimated; it would be ideal to avoid humidity inside the device.

- Calibration must be done with more data sets and for different sky conditions (sunny-cloudy) to compare how the calibration factors change for each condition.

- Calibration must be done with a calibrated device and knowing the sensitivity of the reference data.

- Transmittance of the Hybrid diffuser is not constant over the different wavelengths, it was average over the desired wavelengths ranges, but the accuracy of the estimations could improve if a diffuser with the constant transmission is found.

- Hybrid diffusers are available for customization to better transmittances. With more time, this could be an option to keep good scattering and improve the transmittance.

- Comparison with the grey and white casing should be made blocking the diffuser to estimate the extent to which the temperature difference is due to the diffuser transmittance properties or the colour of the casing.

- Additional tests can be performed outdoors with a metal casing with no ribs to evaluate the extent to which the ribs improve the device's performance in conditions outside the laboratory.

- Prototyped sensors can also be tested in climate chambers, so their resistance to weathering can be assessed and potential problems can then be pinpointed.

- Additional photodiodes and filters can be added to increase the spectral resolution of the sensor.

9. Conclusion

The present work aimed to design and fabricate a spectrally resolved albedometer that estimates the global and reflected irradiance in three different parts of the solar spectrum (320-590nm, 590-850nm, and 850-1100nm). The albedometer consists of two pyranometers, a second version of the solar sensor designed by Annanta Kaul [8]. The sensor's optical, electrical, and mechanical designs were improved throughout the project. Finally, the device was calibrated and validated. There are two configurations of the final prototype. The first configuration consists of the albedometer in a grey aluminium colour with an N-BTK ground glass diffuser. In the in the second configuration, the casing was painted white and had a Hybrid diffuser. The grey sensor operates at temperatures around 17ºC above ambient temperature and has an approximate average error of 20.4%. The white sensor, in comparison, yields irradiance values with an error of 7.3% and has an operating temperature of 8.6ºC above the ambient temperature. Both configurations have a volume of 810cm^2 and cost around €978. The designed spectrally resolved cost-effective albedometer aims to be an accessible solution for an accurate estimation of the power output of bifacial modules and impact the development and implementation of such technologies.

10. Bibliography

[1]   E. Kabir, P. Kumar, S. Kumar, A. A. Adelodun, and K. H. Kim, "Solar energy: Potential and future prospects," *Renew. Sustain. Energy Rev.*, vol. 82, no. September 2017, pp. 894–900, 2018.

[2]   T. C. R. Russell, R. Saive, A. Augusto, S. G. Bowden, and H. A. Atwater, "The Influence of Spectral Albedo on Bifacial Solar Cells: A Theoretical and Experimental Study," *IEEE J. Photovoltaics*, vol. 7, no. 6, pp. 1611–1618, 2017.

[3]   VDMA, "International Technology Roeadmap for Photovoltaic (ITRPV)," 2021.

[4]   R. Guerrero-Lemus, R. Vega, T. Kim, A. Kimm, and L. E. Shephard, "Bifacial solar photovoltaics - A technology review," *Renew. Sustain. Energy Rev.*, vol. 60, pp. 1533–1549, 2016.

[5]   OTT HydroMet B.V., "Albedo measurement for bifacial PV modules," 2018. [Online]. Available: https://www.kippzonen.com/News/847/Albedo-measurement-for-bifacial-PV-modules#.YS5-4y00k_U.

[6]   K. Keegan, "Snow Metamorphism and Firn Compaction," *Ref. Modul. Earth Syst. Environ. Sci.*, 2021.

[7]   M. P. Brennan, A. L. Abramase, R. W. Andrews, and J. M. Pearce, "Effects of spectral albedo on solar photovoltaic devices," *Sol. Energy Mater. Sol. Cells*, vol. 124, pp. 111–116, 2014.

[8]   A. Kaul, "Design and Fabrication of an Irradiance Sensor for PV," 2020.

[9]   T. Park and K. J. Kim, "Determination of an optimal set of design requirements using house of quality," *J. Oper. Manag.*, vol. 16, no. 5, pp. 569–581, 1998.

[10]   Spectrafy, "SolarSIM-ALB Spectral Albedometer," 2021. [Online]. Available: https://www.spectrafy.com/products/solarsim-alb.

[11]   W. R. McCluney, "4. Source/Receiver Flux Transfer Calculations," in *Introduction to Radiometry and Photometry*, 2014, pp. 99–125.

[12]   J. R. Howell, M. P. Menguc, and R. Siegel, "Appendix C : Catalog of Selected Configuration Factors," in *Thermal Radiation Heat Transfer*, 2016, pp. 897–902.

[13]   Edmund Optics, "White diffusing glass." .

[14]   Edmund Optics, "Broadband Hybrid Diffuser."

[15]   W.-C. Wang, "Optical Detectors." Department of Power Mechanical Engineering, National Tsing Hua University., p. 12, 2011.

[16]   Biomimicry Institute, "Cacti stay cool by having ribs that provide shade and enhance heat radiation."

[17]   H. Tributsch, *How Life Learned to Live: Adaptation in Nature*. MIT Press, 1983.

[18]   D. A. Lewis and P. S. Nobel, " Thermal Energy Exchange Model and Water Loss of a Barrel Cactus, Ferocactus acanthodes ," *Plant Physiol.*, vol. 60, no. 4, pp. 609–616, 1977.

[19]   J. D. Mauseth, "Theoretical aspects of surface-to-volume ratios and water-storage capacities of succulent shoots," *Am. J. Bot.*, vol. 87, no. 8, pp. 1107–1115, 2000.

[20]   J. A. Reagan and D. M. Acklam, "Solar reflectivity of common building materials and its influence on the roof heat gain of typical southwestern U.S.A. residences," *Energy Build.*, vol. 2, no. 3, pp. 237–248, 1979.

[21]   "SunCalc." [Online]. Available: https://www.suncalc.org/#/51.9996,4.369,16/2021.08.27/06:46/1.9/1.

[22]   D. L. King, "Improved accuracy for low-cost solar irradiance sensor."

11. Appendix

Correction factors

Table 22: Correction factors for the calculation of irradiance

Correction Factors	Grey-N-BTK	White-Hybrid
%T (320-1100nm)	87%	26%
%T (590-1100nm)	83%	29%
%T (850-1100nm)	83%	23%
S	0.52 W/A	
A	13 mm^2	
VF	99.3%	